

# The QUEST RR Lyrae Survey – III. The low Galactic latitude catalogue

C. Mateu,<sup>1,2\*</sup> A. K. Vivas,<sup>1,3</sup> J. J. Downes,<sup>1,2</sup> C. Briceño,<sup>1,3</sup> R. Zinn<sup>4</sup>  
and G. Cruz-Díaz<sup>5</sup>

<sup>1</sup>Centro de Investigaciones de Astronomía, AP 264, Mérida 5101-A, Venezuela

<sup>2</sup>Escuela de Física, Universidad Central de Venezuela, Apartado Postal 47586, Caracas 1041-A, Venezuela

<sup>3</sup>Visiting Scholar at University of Michigan, Department of Physics, 500 East University, Ann Arbor, MI 48109, USA

<sup>4</sup>Department of Astronomy, Yale University, PO Box 208101, New Haven, CT 06520-8101, USA

<sup>5</sup>Centro de Astrobiología, 28850 Torrejón de Ardoz, Madrid, Spain

Accepted 2012 August 21. Received 2012 August 20; in original form 2012 July 16

## ABSTRACT

We present results for the QUEST RR Lyrae Survey at low Galactic latitude, conducted entirely with observations obtained with the QUEST mosaic camera and the 1.0/1.5-m Jürgen Stock Schmidt telescope at the National Observatory of Venezuela. The survey spans an area of  $476 \text{ deg}^2$  on the sky, with multi-epoch observations in the  $V$ ,  $R$  and  $I$  photometric bands for  $6.5 \times 10^6$  stars in the Galactic latitude range  $-30^\circ \leq b \leq +25^\circ$ , in a direction close to the Galactic anticentre  $190^\circ \leq l \leq 230^\circ$ . The variability survey has a typical number of 30 observations per object in  $V$  and  $I$  and  $\sim 25$  in  $R$ , with up to  $\sim 120$ – $150$  epochs in  $V$  and  $I$  and up to  $\sim 100$  in  $R$  in the best sampled regions. The completeness magnitudes of the survey are  $V = R = 18.5 \text{ mag}$ , and  $I = 18.0 \text{ mag}$ . We identified 211 RR Lyrae stars, 160 bona fide stars of type  $ab$  and 51 candidates of type  $c$ , ours being the first *deep* RR Lyrae survey conducted at low Galactic latitude, in the Galactic disc. The completeness of the RR Lyrae survey was estimated in  $\gtrsim 95$  and  $\sim 85$  per cent for  $RRab$  and  $RRc$  stars, respectively. Photometric metallicities were computed based on the light curves and individual extinctions calculated from minimum light colours for each  $RRab$  star. Distances were obtained with typical errors  $\sim 7$  per cent. The RR Lyrae survey simultaneously spans a large range of heliocentric distances  $0.5 \leq R_{\text{hel}}(\text{kpc}) \leq 40$  and heights above the plane  $-15 \leq z(\text{kpc}) \leq +20$ , with well-known completeness across the survey area, making it an ideal set for studying the structure of the Galactic thick disc.

**Key words:** astronomical data bases: miscellaneous – surveys – stars: variables: RR Lyrae – Galaxy: stellar content – Galaxy: structure.

## 1 INTRODUCTION

In the Milky Way (MW), the thick disc hosts a very old ( $> 10 \text{ Gyr}$ ) and relatively metal poor ( $[\text{Fe}/\text{H}] \sim -0.7$ ) stellar population (Reddy & Lambert 2008; Wyse 2009), comprising  $\sim 10$  per cent or even up to  $\sim 20$  per cent of the thin disc mass (e.g. Jurić et al. 2008). The Galactic thick disc therefore constitutes an important fossil record of the earliest stages of the formation of the Galactic disc, which could help understand the relevant mechanisms contributing to the formation of our Galaxy. From the perspective of galaxy formation, thick discs are remarkably relevant since these have proven to be a ubiquitous component of disc galaxies, as external galaxy surveys have shown that approximately 95 per cent of disc galaxies contain thick discs (Yoachim & Dalcanton 2006).

On the other hand, despite many advances in the last few years, there is no consensus about the formation mechanism of the Galactic thick disc, or even on some fundamental properties of its structure, mainly due to observational difficulties. Scalelength measurements for the MW thick disc range from  $h_r \sim 2$  to  $4.7 \text{ kpc}$  (Chiba & Beers 2000; Larsen & Humphreys 2003; Cabrera-Lavers, Garzón & Hammersley 2005; Carollo et al. 2010), which makes it unclear whether the thick disc is more radially extended than the thin disc or not, or how the density profile behaves at large radii. Another example is metal abundances; the iron abundance of thick disc stars seems to be fairly homogeneous in the vertical direction (e.g. Soubiran, Bienayme & Siebert 2003; Katz et al. 2011), although Chen et al. (2011) recently report an appreciable metallicity gradient. Radial metallicity gradients have not been probed yet and there is also ongoing debate regarding the reach in  $[\text{Fe}/\text{H}]$  at both the low- and high-metallicity tails of the thick disc (Reddy, Lambert & Prieto 2006; Bensby et al. 2007; Reddy & Lambert 2008). In a recent paper, Bovy, Rix & Hogg (2012a) and Bovy et al. (2012b)

\*E-mail: cmateu@cida.vc

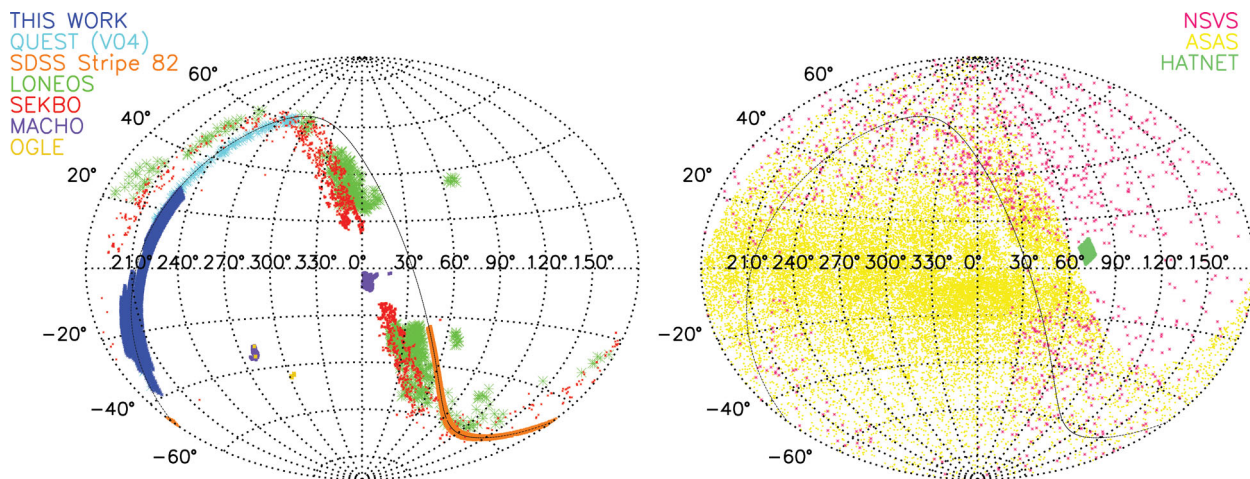


**Figure 1.** Aitoff projection map showing the footprints of recent large-scale RRLS surveys in Galactic coordinates. Left-hand panel: deep surveys ( $V > 16$ ): present survey (blue), QUEST RRLS Survey (cyan), SDSS Stripe 82 (orange), LONEOS (green), SEKBO (red), MACHO (purple) and OGLE (dark yellow). Right-hand panel: shallow surveys ( $V < 16$ ): NSVS (magenta), ASAS-3 (yellow) and HATNET (light green). The solid black line corresponds to the celestial equator. Survey characteristics are summarized in Table 1.

argue against the need of a thin/thick disc decomposition, proposing that the Galactic disc can be described as a series of simple stellar populations having scalelengths and scaleheights which vary smoothly as a function of metallicity and  $\alpha$ -element abundance. This illustrates how the issue of Galactic thick disc structure is far from settled and reliable measurements on structural, kinematic and chemical properties are necessary to gain a better understanding of the MW’s thick disc, which, in turn, will impose strong constraints on the possible contribution of the different formation mechanisms.

Observationally, disentangling the structure of the Galactic disc is a challenging task since the Sun is embedded in it. Numerous studies have been conducted at high Galactic latitudes ( $|b| \gtrsim 30^\circ$ ) in order to study stars at a height above the Galactic plane,  $z \sim 1\text{--}3$  kpc, such that the thin disc density has decayed sufficiently, reducing contamination (e.g. Ojha 2001; Siegel et al. 2002; Brown et al. 2008; Wyse 2009), but also limiting the coverage in the radial direction. At intermediate to low latitudes ( $|b| \lesssim 30^\circ$ ), the problems of crowding and the high and variable extinction become important, and the contribution of the thin disc has to be modelled (Robin et al. 1996; Larsen & Humphreys 2003; Carollo et al. 2010; deJong et al. 2010).

RR Lyrae stars (RRLSs) have several fundamental properties that offer advantages in dealing with these problems inherent to low Galactic latitude observations. RRLSs are *luminosity and colour* standards. Since RRLSs are horizontal branch stars, they have a well-known absolute magnitude which shows little spread (Smith 1995), and allows the computation of distances with small uncertainties ( $\lesssim 10$  per cent, Vivas et al. 2004, hereafter V04). Additionally, during the phase of minimum light of the pulsation cycle, RRLSs of type *ab* have approximately the same effective temperature, and thus show very little dispersion in colour (Sturch 1966; Day et al. 2002). This property enables the use of RR*ab* stars as colour standards to measure extinctions up to the distance of each individual star, which is a crucial point in a low-latitude survey since reddening changes drastically along different lines of sight and has a strong dependence on distance. Also, since RRLSs trace old ( $\gtrsim 10$  Gyr) and mainly metal-poor ( $[\text{Fe}/\text{H}] < -0.5$ ) stellar populations (Smith 1995; Demarque et al. 2000), the expected contamination from the thin disc is negligible (Martin & Morrison 1998).

Finally, RRLSs are pulsating stars with relatively short periods (0.3–1.0 d) and large light-curve amplitudes ( $V \sim 0.3\text{--}1.2$  mag), which makes them easily identifiable by a photometric multi-epoch survey (see e.g. V04; Kinemuchi et al. 2006).

RRLSs have been extensively used as tracers of the Galactic halo by numerous surveys which have studied their spatial distribution in a wide range of distances, from very near the Galactic Centre up to large distances  $R_{\text{gal}} \gtrsim 100$  kpc. This is illustrated in Fig. 1 which shows, in an Aitoff projection map in Galactic coordinates, the footprint of recent large-scale RRLS surveys including the present one. Table 1 summarizes the characteristics of each survey.

Unlike in the Galactic halo, the distribution of RRLSs in the thick disc has been less thoroughly studied, in particular due to the lack of deep RRLS surveys at low/intermediate Galactic latitudes. As illustrated in Fig. 1, the Galactic plane area  $|b| < 20^\circ$  has only been covered by the large-scale yet shallow ( $V < 14$  or  $R_{\text{hel}} \lesssim 5$  kpc) ASAS-3 (Pojmanski 2002) and NSVS (Kinemuchi et al. 2006) surveys, as well as the compilations of nearby RRLSs ( $V \lesssim 13$ ) from Layden (1994, 1995) and Maintz (2005), having been avoided by deep surveys ( $16 < V < 20$ ). This makes ours the first deep large-scale RRLS survey conducted at low Galactic latitudes. Furthermore, our survey probes the outer regions of the thick disc, outside the solar circle. In particular, Layden (1995), Maintz & de Boer (2005) and Kinemuchi et al. (2006, NSVS) have studied the distribution of thick-disc RRLSs in the vertical direction, but the limited coverage at low Galactic latitude prevented the determination of the scalelength as well as the exploration of deviations from an exponential profile such as the *warp* and *flare*, which have been observed in the Galactic thin and thick discs with other tracers (e.g. López-Corredoira et al. 2002; Momany et al. 2006; Hammersley & López-Corredoira 2011). For these reasons, it was essential to conduct a deep RRLS survey at low Galactic latitude, which provided an ample spatial coverage both in the radial and vertical directions.

In this paper, we will present the catalogue of the QUEST<sup>1</sup> RR Lyrae Survey of the thick disc, which spans a total area of  $476 \text{ deg}^2$  at  $-30^\circ < b < +25^\circ$ , with multi-epoch  $V$ ,  $R$ ,  $I$  observations obtained with the 1.0/1.5-m Jürgen Stock Schmidt telescope and the

<sup>1</sup> Acronym for the ‘QUasar Equatorial Survey Team’.

**Table 1.** Characteristics of recent large-scale RRLS surveys in the MW.

Survey	Filters	Area (deg <sup>2</sup> )	Completeness	Telescope	Observatory	Reference
QUEST	<i>VRI</i>	476	$V < 19$	1.0-m Schmidt	NOV	This Work
QUEST (V04)	<i>V</i>	380	$V < 19$	1.0-m Schmidt	NOV	V04
NSVS	ROTSE-NT	~31 000	$V < 14$	4 × 200 mm ROTSE-I	Los Alamos	Kinemuchi et al. (2006)
ASAS-3	<i>V</i>	~31 000	$V < 14$	2 × 200 mm ASAS	Las Campanas	Pojmanski (2002)
LONEOS	LONEOS-NT	1430	$V < 18$	0.6-m Schmidt	Lowell	Miceli et al. (2008)
SEKBO	<i>B<sub>M</sub>R<sub>M</sub></i>	1675	$V < 19.5$	1.27-m MACHO	Mount Stromlo	Keller et al. (2008)
HATNET	<i>I</i>	67	$V < 15$	11-cm HATNET	Fred L. Whipple	Hartman et al. (2004)
OGLE	<i>I</i>	69	$V < 20.5$	1.3-m Warsaw	Las Campanas	Soszynski et al. (2011)
SDSS Stripe 82	<i>ugriz</i>	249	$V < 22$	2.5-m SDSS	Apache Point	Watkins et al. (2009), Sesar et al. (2010)
MACHO	<i>B<sub>M</sub>R<sub>M</sub></i>	~75	$V < 20$	1.27-m MACHO	Mount Stromlo	Kunder & Chaboyer (2008), Alcock et al. (2003)

QUEST mosaic camera, at the National Astronomical Observatory of Venezuela (NOV). In Section 2, we describe the observations and spatial and time coverage of the survey, as well as the photometric processing, error estimation and calibration. In Section 3, we describe the procedures used in the identification of RRLSs, estimate the completeness and possible contamination of the survey and describe the computation of periods, amplitudes, reddenings, photometric metallicities and distances for the identified RRLSs. In Section 4, we summarize the characteristics of our survey. The computation and analysis of RRLS density profiles for the Galactic thick disc and halo will be presented in an upcoming paper of the series.

## 2 THE SURVEY

### 2.1 The data

The present survey spans a total area of 476 deg<sup>2</sup> and makes use of archive observations obtained between late 1998 and mid-2008 with the QUEST camera and the 1.0/1.5-m Jürgen Stock Schmidt telescope at the NOV in Llano del Hato, Venezuela. The camera is a 16 CCD mosaic, with 2048 × 2048 pixel CCDs laid out in a 4 × 4 array, having a field of view of 2.3 × 2.3 deg<sup>2</sup> and a scale of 1.02 arcsec pixel<sup>-1</sup>. The QUEST camera was designed to operate optimally in *drift-scanning* mode and can be fitted with up to four different filters at a time. For a more detailed description of the camera and the drift-scanning technique, see Baltay et al. (2002) and V04.

For the present survey, we used archive drift-scan observations at low Galactic latitudes ( $|b| \lesssim 30^\circ$ ) approximately in the direction towards the Galactic anticentre. These observations were obtained by different observational projects with very different goals, but since the equipment and method of observations are the same as the original QUEST RR Lyrae Survey (V04), we have decided to keep that name for the present survey. Many of the observations indeed come from the QUEST (quasar) survey (Baltay et al. 2002; Rengstorf et al. 2004; V04), and there is also an important number of scans from the CIDA<sup>2</sup> Equatorial Variability Survey (Briceño et al. 2003). The latest spans the equatorial region in the full range of right ascension and has thoroughly surveyed the Orion star-forming region, resulting in a large number of observations in this area (Briceño et al. 2005; Downes et al., in preparation). Our sample is restricted to observations in the range  $60^\circ \leq \alpha \leq 135^\circ$  in right

ascension (corresponding to the range  $190^\circ \leq l \leq 230^\circ$  in Galactic longitude), where the Galactic Plane crosses the celestial equator and drift-scan observations in the declination range  $|\delta| \leq 6.5$  are available.

The observations were obtained using different filter combinations and have different spatial coverage and cadence, all of which changed over time, resulting in a highly inhomogeneous sample. The survey is composed of 452 drift-scans corresponding to 19 238 h of observation and 6.3 Tb of data in the *V*, *R* and *I* photometric bands, obtained in a total of 427 nights between 1998 December and 2008 June. Although ideally an RRLS survey would use a blue filter, since the amplitudes of variation of RRLSs would be larger, we did not include these observations in our sample since these were very few due to the low sensitivity of QUEST CCDs in this band.

The present survey includes the low Galactic latitude observations from the RRLS survey of V04, which consisted of QUEST drift-scans at  $\delta = -1^\circ$  obtained between 1998 December and 2001 April. This results in an overlap area of 90 deg<sup>2</sup> at both ends of the present survey (see Fig. 1) in the right ascension ranges  $60^\circ \leq \alpha \leq 90^\circ$  and  $120^\circ \leq \alpha \leq 135^\circ$  and the declination range  $-2^\circ \leq \delta \leq 0^\circ$ . New observations (post-2001) were added in this area and the existing ones from V04 were reprocessed using the procedures described in the following section, which were devised to make an optimal use of data in the three available filters *V*, *R*, *I*. Finally, data in the range  $60^\circ \leq \alpha \leq 90^\circ$  are also part of the CIDA Deep Survey of Orion (Downes et al., in preparation).

### 2.2 Data reduction and photometry

In the following sections, we will describe the procedures used in the object detection, astrometric reduction, aperture and point spread function (PSF) photometry.

#### 2.2.1 Object detection, astrometry and aperture photometry

Each individual drift-scan observation was reduced using OFFLINE, the standard pipeline developed by the QUEST collaboration (Baltay et al. 2002). The OFFLINE pipeline automatically performs basic reductions, object detection, aperture photometry and astrometric reductions for each image frame in a drift-scan observation. This processing was conducted independently for the images obtained by each of the camera's CCDs, resulting in 16 independent catalogues having positions in celestial equatorial coordinates, photometric magnitude and error for each point source, as well as

<sup>2</sup> Acronym for the ‘Centro de Investigaciones de Astronomía’

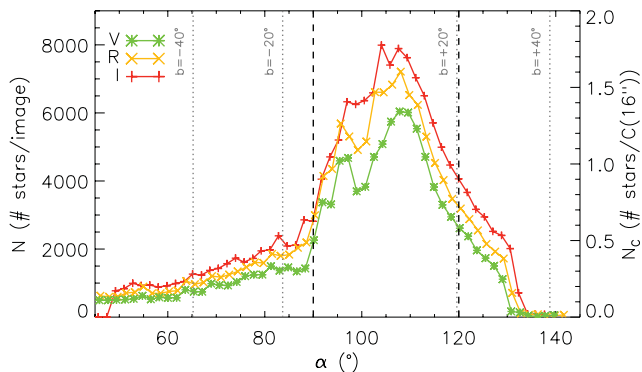


**Figure 2.** Number of stars per image as a function of  $\alpha$ , for a drift-scan centred at  $\delta = -3^\circ$ , with the filters  $V$ ,  $R$  and  $I$  (\*,  $\times$  and  $+$ , respectively). The right-hand vertical axis indicates the typical number of stars  $N_C$  inside a circle of radius 16 arcsec [ $C(16 \text{ arcsec})$ ]. The dotted grey lines indicate the regions corresponding to the Galactic latitudes  $b = \pm 20^\circ, \pm 40^\circ$ . The black dashed lines delimit the region where PSF photometry was computed.

(photometric parameters such as full width at half-maximum (FWHM), ellipticity, sky background flux and error, etc.

Image reduction consists of standard bias, dark and flat-fielding corrections. Object detection is made at the  $3\sigma$  level and aperture photometry is performed over all detected point sources with an aperture radius of 1 FWHM. The astrometric matrices are computed using the USNO-A2 (Monet 1998) astrometric catalogue as a reference. The astrometric solutions computed by OFFLINE have a typical accuracy of  $\sim 0.15$  arcsec, which is sufficient for the cross-identification of an object in the different catalogues.

### 2.2.2 PSF photometry

Since our drift-scan observations include very crowded regions at low Galactic latitude, the use of PSF photometry was necessary. Fig. 2 shows a plot of the typical number of stars per image in the  $V$ ,  $R$  and  $I$  bands, as a function of right ascension  $\alpha$  for a drift-scan at  $\delta = -3^\circ$  which spans the entire right ascension range covered by this survey. The right-hand vertical axis shows the scale in terms of  $N_C$ , the number of stars in a circle with a 16 arcsec radius (which is twice the aperture diameter in an observation with a bad seeing of 4 arcsec). The plot illustrates how the number of objects per image increases when approaching the Galactic plane. In particular  $N_C > 1$  in the range  $95^\circ \lesssim \alpha \lesssim 115^\circ$ , meaning that the typical separation between two objects in an image is less than twice the aperture diameter and therefore aperture photometry for most stars will be contaminated by neighbours. Therefore, the computation of PSF photometry was restricted to the right ascension range  $90^\circ \leq \alpha \leq 120^\circ$ , in which  $N_C \gtrsim 0.8$  (indicated in Fig. 2 with the dashed black lines). In low-density areas, consistency was checked by computing both aperture and PSF photometry.

PSF photometry was obtained using the standard DAOPHOT (Stetson 1987) routines implemented in IRAF,<sup>3</sup> tied together in an automated pipeline called OFFLINEPSF, which is customized for QUEST drift-scan observations.

OFFLINEPSF includes as a first step, prior to the computation of PSF photometry, the re-centring and recomputation of aperture pho-

tometry for all point sources previously detected with OFFLINE. This is necessary since initial OFFLINE detections have centring errors of  $\sim 1$  pixel, which are reduced to  $\sim 0.1$  pixel by using PHOT’s recentring options. Using the recalculated centroids and aperture photometry magnitudes, PSF photometry is obtained according to an iterative scheme where, for each individual image, input parameters such as the fit radius  $r_{\text{fit}} = 1 \times \text{FWHM}$  and the model PSF radius  $r_{\text{psf}} = 3 \times r_{\text{fit}}$  are computed independently. Then, from 90 to 120 PSF stars are selected, uniformly distributed across the image, without neighbours within a radius  $r_{\text{psf}}$  and, for distances less than  $2r_{\text{psf}}$  requiring neighbours be at least 1 mag fainter and there are no bad pixel columns near. An initial PSF model is made with the DAOPHOT PSF task, with a second-order spatial variation across the image. The PSF model is fitted around PSF stars with the NSTAR and SUBSTAR tasks, PSF stars with newly detected neighbours are discarded and the PSF model recomputed. The PSF model is then fitted to all point sources in the entire image using ALLSTAR and new objects are detected if present in the resulting subtracted frame, iterating twice more over these two steps.

The OFFLINE and OFFLINEPDF processes result, for each drift-scan, in a photometric catalogue per CCD, containing the equatorial coordinates  $\alpha$ ,  $\delta$ , instrumental aperture and PSF magnitudes and errors, for each point-source object detected in the full drift-scan.

### 2.2.3 Photometric calibration

The photometric calibration was done in two stages: the calibration of a *master catalogue* by means of second-order photometric standards and the normalization of individual drift-scan observations to this master photometric catalogue.

The *master catalogue* is composed of three to four individual scans per declination stripe, observed with good and constant seeing and sky background throughout the whole duration of the scan. The combination of these scans allowed for a much more homogeneous master catalogue than would have been obtained if only one scan had been used, due to empty regions caused by bad columns and defective regions of the CCDs. The *master catalogue* obtained contains 6 513 705 objects and its coverage is illustrated in the density map shown in Fig. 3.

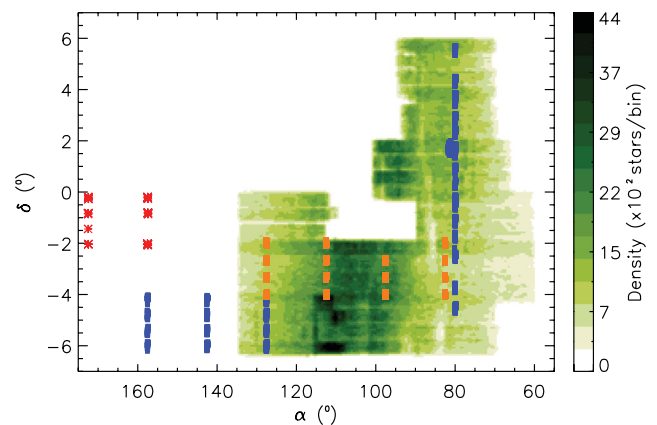


**Figure 3.** Density map of stars in the master photometric catalogue and spatial distribution of second-order photometric standards used for photometric calibration. The grey-scale represents stellar density as indicated by the colour bar, per  $0.24 \text{ deg}^2$  bin (equivalent to half the area of a QUEST CCD). The dots indicate the positions of second-order photometric standards established by different authors: Downes et al. (in preparation) (blue), V04 (red) and this work (orange).

<sup>3</sup> IRAF is distributed by the National Optical Astronomy Observatories, which are operated by the Association of Universities for Research in Astronomy, Inc., under cooperative agreement with the National Science Foundation.

**Table 2.** Magnitudes for second-order photometric standards. (This table is published in its entirety as Supporting Information with the electronic version of the article. A portion is shown here for guidance regarding its form and content.)

ID	$\alpha$ ( $^{\circ}$ )	$\delta$ ( $^{\circ}$ )	$V$ (mag)	$R$ (mag)	$I$ (mag)
ss4000	82.401749	-2.04192	13.446 $\pm$ 0.003	12.238 $\pm$ 0.003	12.822 $\pm$ 0.003
ss4001	82.420319	-2.10225	14.386 $\pm$ 0.005	13.201 $\pm$ 0.005	13.800 $\pm$ 0.004
ss4002	82.431961	-2.04361	16.905 $\pm$ 0.020	14.526 $\pm$ 0.009	15.849 $\pm$ 0.012
ss4003	82.436493	-2.11058	16.630 $\pm$ 0.018	15.197 $\pm$ 0.014	15.912 $\pm$ 0.012
ss4004	82.437607	-2.03612	16.784 $\pm$ 0.019	15.329 $\pm$ 0.015	16.046 $\pm$ 0.013

The instrumental magnitudes for each object in the *master catalogue* were calibrated using second-order photometric standards. A total of 4526 photometric standards were used, spanning the magnitude range  $10 < V < 17$  with colours  $-0.2 < V - R < 1.2$ , and identified as non-variable stars in any one of the *VR* bands, with a spatial distribution illustrated in Fig. 3. Photometric standard stars indicated by the black dots (2621 in total) were set up by Downes et al. (in preparation) using observations obtained with the 1.2-m telescope and the Keplercam camera, at the Fred L. Whipple Observatory, Mt. Hopkins, USA. The asterisks indicate the 28 standards having  $\delta = -1^{\circ}$  and  $\alpha < 175^{\circ}$ , established by V04 with observations from the 1.0-m YALO<sup>4</sup> telescope at the Cerro Tololo Interamerican Observatory (CTIO), Chile. Finally, as part of this work, we established 1877 second-order standards in the range  $-4^{\circ} \leq \delta \leq -2^{\circ}$  (denoted in Fig. 3 by the dark grey dots), using observations obtained during 2004 December, with the 0.9-m SMARTS<sup>5</sup> telescope at CTIO. Data for these 1877 second-order standards are summarized in Table 2. The photometric calibration was performed independently in declination stripes having the width of a QUEST CCD and in 1-h-long intervals in right ascension where the distribution of standards allowed it. The catalogue regions centred around  $\delta = -1^{\circ}$  with  $110^{\circ} \leq \alpha \leq 135^{\circ}$  and  $\delta < -5^{\circ}$  with  $\alpha > 130^{\circ}$  lacked photometric standard stars, so these were calibrated using long reference scans which extended as far as the area covered by the V04 standards (asterisks) and Downes et al. (in preparation) (black dots), respectively.

The photometric solutions for each scan were obtained using zero-point and  $V - R$  or  $V - I$  colour terms, depending on the filters available for each observation. A mean photometric precision of  $\sim 0.021$  mag was achieved for the  $V$ ,  $R$  and  $I$  bands.

#### 2.2.4 Normalization

The master photometric catalogue, described in the previous subsection, provides the calibrated reference photometry for all survey objects. The individual observations, used to construct time series for each object (see Section 3.2) used in the RRLS search, were calibrated by normalizing each scan to the master reference catalogue.

The normalization process, taken from V04, consists of identifying all objects of a particular scan in the reference master catalogue and computing the mean magnitude residuals in both, throughout the whole scan in 0.25 arcmin bins in right ascension. Since most stars ( $\gtrsim 95$  per cent) are non-variable and the number of stars in each bin is sufficiently large ( $\sim 1500$ – $3000$ ), the average residuals

obtained result in a precise estimation of the zero-point needed to calibrate each bin of the scan. This normalization process allows for the correction of systematic trends in the magnitude residuals caused by changes in the atmospheric conditions during each observation, which in our case is critical, given that a single drift-scan can be up to 7 to 8 hours long (see fig. 3 in V04, for an example of the normalization process). The typical resulting standard deviation of the residuals in each bin was  $\sim 0.015$  mag, giving zero-point errors  $\sim 0.002$  mag.

#### 2.2.5 Photometric errors

Taking advantage of the fact that each star in our survey has multiple observations in each filter, it is suitable to use the standard deviation  $\sigma$  of magnitudes of non-variable stars as the representative photometric error in the given filter. Since the majority of stars in any given field are non-variable, these give rise to the main trend in a plot of  $\sigma$  versus mean magnitude, as seen in Fig. 4.

In the figure, the crosses show the average standard deviation computed as a function of mean magnitude in 0.5 mag bins using an iterative  $3\sigma$  clipping. The sharp increase in  $\sigma$  for objects brighter than  $V \sim 14.5$  mag is due to objects saturated in most observations. This behaviour provided us with a means to empirically determine the saturation magnitude and, for each object, remove the individual observations brighter than this limit. The solid line indicates a

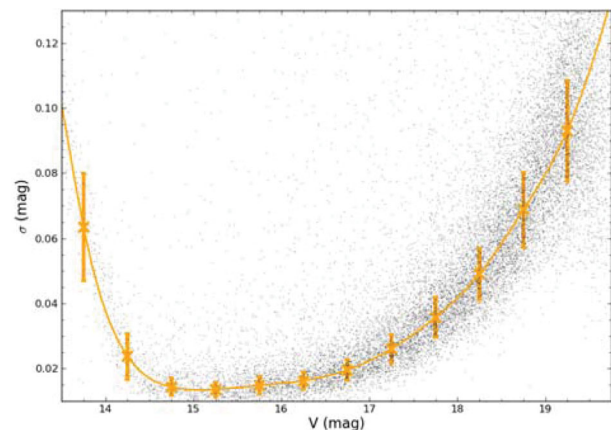


**Figure 4.** Magnitude standard deviation  $\sigma$  as a function of mean  $V$  magnitude, for stars in a typical  $0.5 \times 15$  deg<sup>2</sup> region centred around  $(\alpha, \delta) = (85^{\circ}, +3^{\circ})$ , with a mean number of  $\sim 25$  observations per star. The solid line indicates the polynomial fit of the average  $\sigma$  in 0.5 mag bins, as a function of mean magnitude. The error bars indicate the standard deviation around each of these averages.

<sup>4</sup> Acronym for ‘Yale Aura Lisbon Ohio’.

<sup>5</sup> Acronym for ‘Small and Moderate Aperture Research Telescope System’.

**Table 3.** Saturation, completeness and limiting magnitudes of the survey.

Filter	$m_s$ (mag)	$\Delta m_s$ (mag)	$m_c$ (mag)	$\Delta m_c$ (mag)	$m_l$ (mag)	$\Delta m_l$ (mag)
<i>V</i>	14.0	0.018	18.5	0.064	19.70	0.15
<i>R</i>	14.0	0.018	18.5	0.072	19.75	0.15
<i>I</i>	13.5	0.020	18.0	0.078	18.80	0.15

polynomial fit of the average  $\sigma$  versus magnitude (crosses) and the error bars correspond to the standard deviation around this average. The polynomial fit consequently provides the typical magnitude standard deviation due to photometric uncertainties only, as a function of an object’s mean magnitude, which we assumed as its photometric error.

For each survey star, we computed the corresponding photometric error as the typical magnitude standard deviation given by the polynomial fit, for the corresponding mean magnitude. This error analysis was conducted independently for observations in each of the *V*, *R* and *I* filters and dividing the entire survey in separate regions of  $\Delta\delta = 0.5$  times  $\Delta\alpha = 15^\circ$ .

### 2.3 The photometric catalogue

The final photometric catalogue spans a total area of 476 deg<sup>2</sup> having 6 513 705 objects with multi-epoch observations in the *V*, *R* and *I* bands. Table 3 summarizes the saturation ( $m_s$ ), completeness ( $m_c$ ) and limiting ( $m_l$ ) magnitudes in the three photometric bands, as well as the typical errors corresponding to these magnitudes.

The spatial coverage of the survey as well as the typical number of epochs per object, in each of the photometric bands, are illustrated in Fig. 5 in equatorial coordinates. As can be seen in the figure, the number of observations per object goes from  $\sim 10$  up to  $\sim 150$  in the *V* and *I* bands and up to  $\sim 60$  in the *R* band. The number of epochs per star per filter is quite inhomogeneous throughout the survey, as illustrated by Fig. 5; nevertheless most objects have at least 10 observations in two photometric bands, while objects in the thoroughly sampled Orion region have more than  $\sim 30$  observations in each of the *V*, *R* and *I* bands.

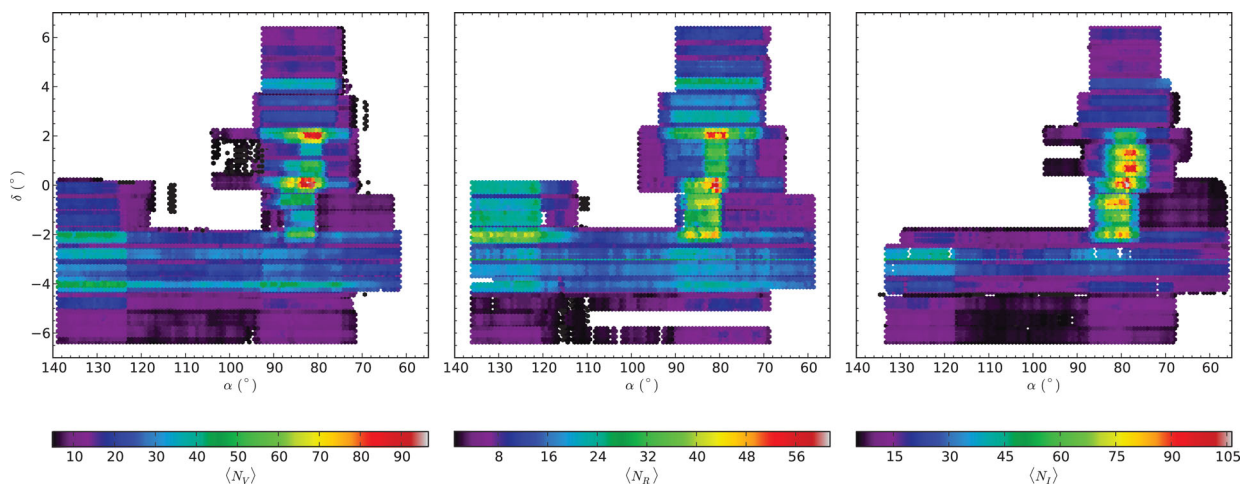
## 3 THE RR LYRAE SEARCH

### 3.1 Light-curve simulations

The present survey has very inhomogeneous time sampling and number of epochs in the different filters, which in turn change in different regions of the survey. These differences can have a sizeable impact in the completeness of the resulting RRLS sample, which must be properly characterized. We used light-curve simulations as a tool to test and fine-tune the variable star detection and period searching techniques used to identify RRLS stars (Sections 3.2 and 3.3.1), as well as to characterize the completeness of the *RRab* and *RRc* samples as a function of position in the survey (Section 3.3.5).

A total of 425 000 synthetic light curves were generated for RRLSs of each type, *ab* and *c*, and the same number for non-variable stars. The time sampling and photometric errors as a function of magnitude (see Section 2.2.5) were taken from actual objects uniformly distributed throughout the entire survey area. This ensures a truly representative realization of the time spacing, the number of observations per filter and the number of quasi-simultaneous observations in different filters, for each synthetic object. This point is of particular importance, given the differences both in the cadence and spatial coverage in the different photometric bands as a function of position, as illustrated in Fig. 5.

The parameters used to create synthetic light curves for *RRab* and *RRc* stars are summarized in Table 4. We generated synthetic stars with random mean *V* magnitudes ( $\langle V \rangle$ ) uniformly distributed in the range [13.0, 20.0]. For each object, the corresponding mean magnitudes ( $\langle R \rangle$ ) and ( $\langle I \rangle$ ) were computed from the mean  $V - R$  and  $V - I$  colours, randomly drawn from Gaussian distributions with means and standard deviations taken from Alcock et al. (2003), indicated in Table 4. The pulsation period  $P$  of each object was randomly drawn from a Gaussian distribution and the *V*-band amplitude computed from the (Oosterhoff I) period–amplitude relation from Cacciari, Corwin & Carney (2005), with random Gaussian noise with  $\sigma = 0.12$  mag, for *RRab* stars. For *RRc* stars, since the period–amplitude relation is weak, the *V*-band amplitude was randomly drawn from a Gaussian distribution assuming a mean standard deviation taken from V04 (see Table 4). This way our simulated population of RRLSs shows the period–amplitude trend for Oosterhoff I *RRab* stars (which represent  $\sim 80$  per cent of all *RRab* stars in the


**Figure 5.** Spatial coverage of the survey in the *V* (left-hand panel), *R* (middle panel) and *I* (right-hand panel) bands. The colour bars indicate the mean number of epochs per object in each filter.

**Table 4.** Parameters used in the simulation of RR*ab* and RR*c* light curves.

Parameter	RR <i>ab</i>	RR <i>c</i>	Reference
$\langle P \rangle$	0.539 d	0.335 d	V04
$\sigma P$	0.09 d	0.07 d	V04
$\langle \text{Amp}V \rangle$	1.04 mag	0.536 mag	V04
$\sigma_{\text{Amp}V}$	0.24 mag	0.13 mag	V04
$\text{Amp}R$	$0.74064 \times \text{Amp}V + 0.0361$		Alcock et al. (2003)
$\text{Amp}I$	$0.66800 \times \text{Amp}V + 0.0501$		Dorfi & Feuchtinger (1999)
$\langle V \rangle$	13.0–20.0		–
$(\langle V - R \rangle, \sigma_{V-R})$	(0.30, 0.26)		Alcock et al. (2003)
$(\langle V - I \rangle, \sigma_{V-I})$	(0.42, 0.20)		Alcock et al. (2003)

Galactic halo, e.g. Sesar et al. 2010), albeit not the Oosterhoff dichotomy. Note that although we do not simulate the Oosterhoff dichotomy, nor the Blazhko effect (an amplitude modulation known to occur in some RRLSs, e.g. Kovacs 2009), we do not expect they will affect our completeness estimates for the survey. For a given period, Oosterhoff II stars would have even larger amplitudes than Oosterhoff I ones making them even easier to identify. On the other hand, the amplitude of RRLSs is large enough such that the (relatively small) variations due to the Blazhko effect will only translate in the light curves appearing slightly more noisy.

Given the  $V$ -band amplitude ( $\text{Amp}V$ ), the corresponding amplitudes in the  $R$  and  $I$  bands were computed according to the linear relationships from Dorfi & Feuchtinger (1999), and Alcock et al (1999) and Alcock et al. (2003), respectively, including the Gaussian uncertainty estimated for these relationships. This procedure correctly reproduces the amplitude ratios observed for RRLSs in different photometric bands (e.g. Smith 1995; Sterken & Jaszchek 2005). Finally, an initial phase offset randomly drawn from a uniform distribution in the  $\phi \in [0, 1)$  range was added to the synthetic light curve of each object which in turn was sampled from RR*ab* or RR*c* light curve templates from Layden (1998) and Vivas et al. (2008), respectively, in order to obtain the magnitudes corresponding to each epoch of observation (in each filter). A random Gaussian photometric uncertainty was added to each of the synthetically produced magnitudes, using the error versus magnitude curves for each filter derived for the survey (see Section 2.2.5).

Time series data were also generated for synthetic non-variable stars with  $\langle V \rangle \in [13.0, 20.0]$ . Mean ( $R$ ) and ( $I$ ) magnitudes were computed from  $V - R$  and  $V - I$  colours, randomly drawn from uniform distributions in the ranges  $[-0.1, 1.5]$  and  $[-0.2, 3.0]$ , respectively, which correspond to the entire  $V - R$  and  $V - I$  colour range for main-sequence stars according to Kenyon & Hartmann (1995).

### 3.2 Variable star identification

The first step in the search for RRLSs consisted of identifying variable stars, by means of the variability indices defined by Stetson (1996).

The  $J$  and  $K$  variability indices were initially defined by Welch & Stetson (1993) and later modified and combined by Stetson (1996) in the definition of the  $L$  index, specifically designed for the automated identification of pulsating variables and the reduction of contamination due to spurious variables caused by deviant photometric observations. The definition of the  $L$  index uses the

fact that, for pulsating stars, quasi-simultaneous observations in two photometric bands must experience deviations (with respect to the corresponding means) which show a positive correlation, as opposed to non-variable stars for which this deviations would be uncorrelated.

The QUEST drift-scans comprising this survey have data in up to four different filters (see Section 2.3) obtained almost simultaneously, since the mean separation between observations in two different filters is  $\Delta t \sim 2\text{--}6$  min (given by the time it takes an object to cross the different CCD rows of the camera), which compared to the typical period of an RRLS star ( $P \sim 0.55$  d) can be considered negligible ( $\Delta t/P \sim 7 \times 10^{-3}$ ). This makes it an ideal set of observations to use Stetson's variability indices.

Candidate variable stars were identified based on the three Stetson  $L$  indices that can be computed with our observations, that is,  $L_{VR}$ ,  $L_{VI}$  and  $L_{RI}$ . Given that the survey coverage and sampling are very inhomogeneous in the different filters (see Fig. 5), the criteria used in identifying variable stars needed to be sufficiently flexible in order to consider, for example, objects that have observations in any two bands and not the third, yet without seriously reducing the completeness in the process. Therefore, we selected as candidate variable stars those objects having at least one of the three possible  $L$  indices greater than a threshold value of 1, slightly higher than the threshold value 0.9 used by Stetson (1996) in the identification of Cepheid variables. This threshold value was chosen based on results from light-curve simulations of RR*ab*, RR*c* and non-variable stars with the survey's time sampling.

A plot of  $L_{VR}$  as a function of  $V$  is shown in Fig. 6 (left-hand panel). As expected, the larger amplitude RR*ab* stars (blue dots) have on average larger  $L$  values than the lower amplitude RR*c* stars (green dots), while non-variable (black dots) stars have  $L$  values around 0. The criteria used to select variable star candidates (at least one  $L$  index higher than 1, see Section 3.2) ensure there will be negligible contamination from non-variable and low-amplitude ( $\lesssim 0.2$  mag) variable stars, while still recovering most variable stars, regardless of whether these have a small number of observations ( $\lesssim 10\text{--}12$ ) in some filters. The completeness of the variable candidate sample achieved using these criteria is illustrated as a function of mean  $V$  magnitude in Fig. 6 (right-hand panel). Within the saturation and completeness magnitude limits (dashed lines), the completeness in the variable star identification was estimated in 99.1 per cent for RR*ab* and 98.3 per cent for RR*c* stars.

Using these criteria, we obtained a sample of 486 766 candidate variable stars, corresponding to 7 per cent of the total number of stars in the survey.

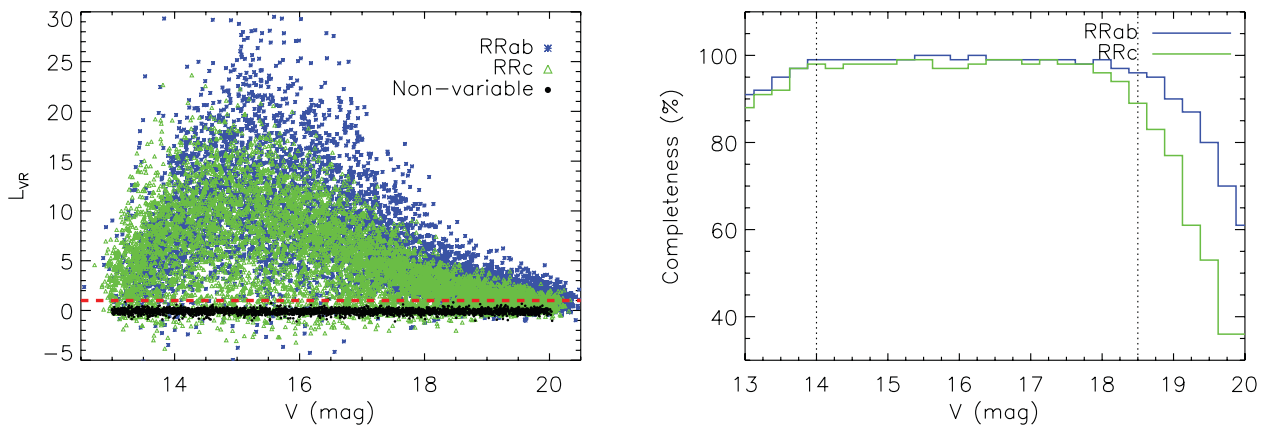


**Figure 6.** Left-hand panel:  $L_{VR}$  versus  $V$  magnitude, for synthetic non-variable (black), RRab (\*) and RRc (triangle) stars. The dashed line indicates the threshold chosen for the selection of variable stars. Right-hand panel: completeness of the variable star identification, estimated from synthetic light curves of RRab (blue) and RRc (green) stars. The dotted lines indicate the survey’s saturation and completeness magnitudes in the  $V$  band (see Table 3).

### 3.3 RR Lyrae identification

#### 3.3.1 Period search

The search for RRLSs was conducted using a version of the Lafler & Kinman (1965) method for the identification of periods of variable stars, modified by Stetson (1996) and extended in the present work in order to incorporate the information of multi-filter time series data.

The method consists of computing, for a series of trial periods, the parameter

$$S(M) = \frac{\sum_i^{N_M} \omega(i, i+1) |m_i - m_{i+1}|}{\sum_i^{N_M} \omega(i, i+1)}, \quad (1)$$

where  $m_i$  and  $m_{i+1}$  are consecutive magnitudes in the  $M$  filter, in the light curve folded with the trial period,  $N_M$  is the number of observations and  $\omega(i, i+1)$  are weights proportional to the magnitude errors  $\sigma_i$ , given by

$$\omega(i, i+1) = \frac{1}{\sigma_i^2 + \sigma_{i+1}^2}. \quad (2)$$

The true period corresponds to the minimum  $S(M)$ , since the light curve is smooth when folded with the correct period and therefore the sum of differences between consecutive magnitudes is minimal. Since  $S(M)$  considers only the data in the  $M$  filter, in order to incorporate the information available for each object in all three  $V$ ,  $R$  and  $I$  filters, we used the composite index  $S_{VRI}$  as the average of the  $S(M)$  for each filter (see e.g. Watkins et al. 2009), weighted by the corresponding number of observations, as given by

$$S_{VRI} = \frac{N_V S(V) + N_R S(R) + N_I S(I)}{N_V + N_R + N_I}, \quad (3)$$

where  $N_V$ ,  $N_R$  and  $N_I$  correspond to the number of observations in each of the  $V$ ,  $R$ ,  $I$  filters, respectively. By minimizing the  $S_{VRI}$  parameter given by equation (3), we are using the data in all the available filters, requiring that the best period be the one that smoothes the period-folded light curves in the three photometric bands.

RRLSs are known to exhibit a narrow range in temperature, and therefore colour, which is why the use of colour cuts is frequent in RRLS searches (e.g. V04; Ivezić et al. 2005). However, in low galactic latitude surveys, stars are severely affected by strong and highly variable extinction, and the use of colour cuts is better avoided in order to ensure the survey’s completeness, albeit increasing the

computational cost of conducting the period search over a much larger sample. Therefore, the period search was conducted over the full sample of 486 766 variable candidates selected without imposing any sort of colour cuts. The search spanned the period range from 0.2 to 1.2 d with a  $10^{-4}$  d period step and for each star, and a second-order search was performed with increased period resolution around the five best periods initially found, using a period step of  $10^{-5}$  d. The best three periods found after the refined search were reported for each object characterized by a statistical significance parameter  $\Lambda$  defined as

$$\Lambda = \frac{S_{VRI}(P) - \langle S_{VRI} \rangle}{\sigma(S_{VRI})}, \quad (4)$$

where  $\langle S_{VRI} \rangle$  and  $\sigma(S_{VRI})$  are the mean and standard deviation of the distribution of  $S_{VRI}$  values for all trial periods.

#### 3.3.2 Period aliases

The emergence of *alias* or *spurious* periods is a common problem when trying to identify the period of a signal from time samplings which may or may not be uniform. In general, these can simply be harmonics of the true period or they can come up as a consequence of an underlying periodicity in the time sampling, being therefore external to the signal itself. Following Lafler & Kinman (1965) we can express the relationship between the true period  $P$  and spurious periods  $\Pi$  as

$$\frac{1}{\Pi} = \frac{k}{P} + \frac{1}{p}, \quad (5)$$

where  $k$  is a rational number, which produces the true period harmonics, and  $p$  is the external period of the sampling. As noted by Lafler & Kinman (1965) the external periods  $p$  of interest are those which produce period aliases in the expected range of the signal, in this case in the period range of RRLSs, since the rest can be ruled out on physical grounds.

In the present case of the RRLS search, the typical 1-d periodicity between the drift-scan observations composing our survey leads to the emergence of spurious periods in the range  $0.2 \lesssim P(\text{d}) \lesssim 1$  expected for RRLSs. This spurious periods, commonly termed one-day aliases, are obtained from equation (5) with  $p = \pm 1$  and  $k = 1$ . Other period aliases can arise due to underlying periodicities in the time sampling, as a consequence of the inhomogeneity in the time sampling of our survey.



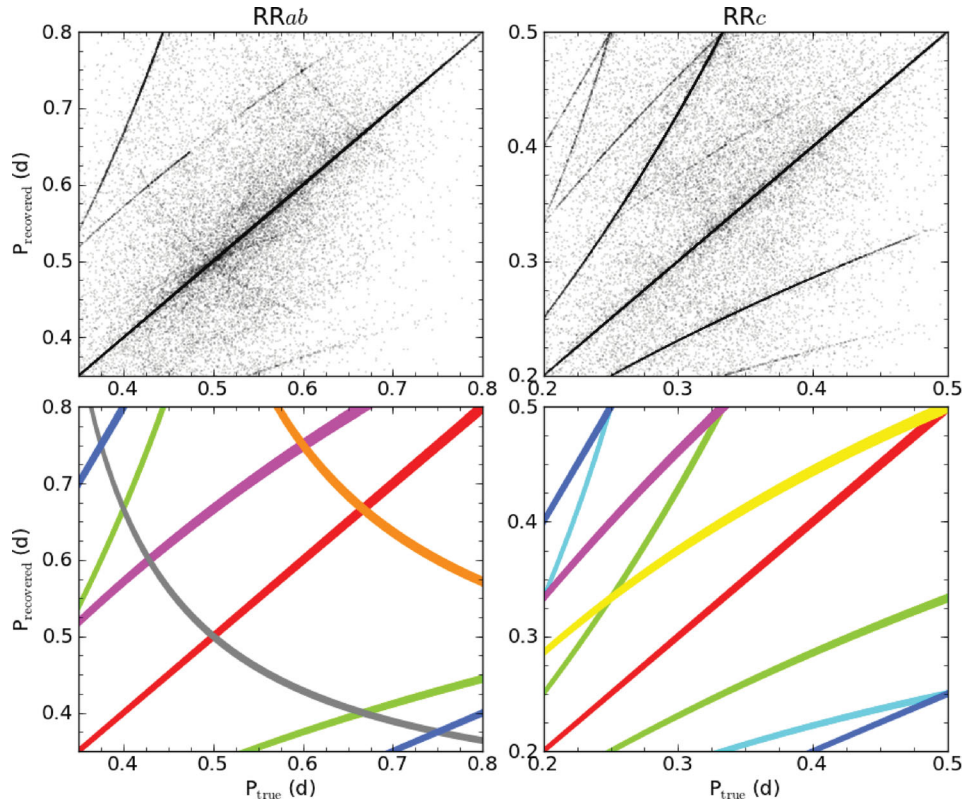


**Figure 7.** Top panels: recovered versus true period for synthetic stars: *RRab* (left-hand panel) and *RRc* (right-hand panel). Bottom panels: loci defined by the period aliases visible in the top panels. The shaded red area indicates the identity locus. The remaining areas indicate the loci of the most common alias periods: one-day aliases (green),  $2 \times P_{\text{real}}$  and  $0.5 \times P_{\text{real}}$  (blue),  $2 \times$  one-day aliases (magenta),  $1/2$ -day aliases (cyan),  $1/3$ -day aliases (orange),  $1/4$ -day aliases (grey) and  $2 \times 1/2$ -day alias (yellow). The shaded areas have a width equal to 2 per cent separation from the corresponding locus. Note that, in the top panels, the points lying within the identity locus correspond to 80 and 46 per cent of the total synthetic *RRab* and *RRc* samples, respectively.

**Table 5.** Occurrence frequency of alias periods.

Type	$k$	$p$ (d)	Frequency (per cent)		Colour
			<i>RRab</i>	<i>RRc</i>	
1-day alias	1	+1	11.9	13.1	Green
	1	-1	28.4	36.2	Green
$1/2$ -day alias	1	+1/2	1.9	1.6	Cyan
	1	-1/2	-	6.1	Cyan
$1/3$ -day alias	-1	1/3	12.6	-	Orange
$1/4$ -day alias	-1	1/4	17.4	-	Grey
Harmonics	2	$\infty$	8.4	7.7	Blue
	$1/2$	$\infty$	1.7	0.4	Blue
1-day alias harmonic	$1/2$	-1/2	-	15.4	Yellow
$1/2$ -day alias harmonic	$1/2$	-1/4	17.7	19.4	Magenta

In order to empirically identify the most frequent alias periods in our sample, we conducted the period search described in the previous section, over the synthetic time series data for  $\sim 130\,000$  of our simulated *RRab* and *RRc* stars (see Section 3.1). Fig. 7 shows plots of the recovered period as a function of the true period for synthetic *RRab* (left-hand panel) and *RRc* (right-hand panel) stars. The most populated sequence in the plot is the identity, indicated by the red shaded area. Different alias periods given by equation (5) match the other sequences observed in Fig. 7. The most prominent loci defined by the alias periods identified in the sample are shaded in different colours, as detailed in Table 5. The width of the shaded

loci in Fig. 7 indicates a separation smaller than 2 per cent from the corresponding main locus.

Fig. 7 shows that the majority of the periods lie in the identity locus. If the recovered period differs by less than 10 per cent from the true period, we consider it correctly recovered, with this definition we find that for *RRab* stars 80 per cent of the times the period is recovered, while for *RRc* stars it is only  $\sim 46$  per cent. For the majority of the remaining stars, the recovered period is an alias of the true period. This indicates, as can be seen in the figure, that the fraction of *RRc* stars affected by spurious periods is much larger than that for *RRab* stars. The frequency of occurrence of the alias periods indicated in Fig. 7 is summarized in Table 5, for both types of RRLSs, computed from  $\sim 130\,000$  simulated *RRab* and *RRc* light curves. As can be seen both in the table and in Fig. 7, one-day aliases are the most frequent as noted by Lafler & Kinman (1965). Nevertheless, other spurious periods can arise, albeit less frequently, such as the  $1/3$ -day and  $1/4$ -day aliases for *RRab* stars and the  $1/2$ -day alias and first harmonic of the true period for *RRc* stars.

This empirical overview of the most frequent spurious periods, obtained by means of the simulated light curves, enabled us to quantify the relative importance of the different possible aliases present in our RRLS survey. Based on these results, an inspection of the identified period aliases was included in the period search, described in the previous subsection, during the visual inspection of the period-folded light curves. This allowed increasing the completeness in the RRLS identification, which is described in the following section.

### 3.3.3 Final selection of RRLSs

We visually inspected the light curves for the 66 086 stars for which a statistically significant ( $\Lambda \geq 3.0$ ) minimum of  $S_{VRI}$  was found. The visual inspection and classification of light curves was done using the plotting tool `INSPECTLC.PY`, developed as part of this work, whose graphical user interface is shown in Fig. 8. The `INSPECTLC.PY` program allows visualizing, for each star, light curves in three different filters (in this case  $V, R, I$ ) period folded with each of the three most significant periods found. These light curves are shown in Fig. 8 under the labels P1, P2 and P3. The text box to the left-hand side of the window summarizes each star's parameters: identification number,  $\alpha, \delta$ , amplitude and number of observations in each of the three filters, the three best periods ( $P_i$  with  $i = 1, 2, 3$ ) and their corresponding values of  $\Lambda$ . The 'TRY ALIAS' button displays, for a given period  $P_i$ , the period-folded light curves using five of the most common alias periods (see Table 5) plus one user-defined alias, computed from the values inserted in the 'k' and '1/p' text boxes (see Section 3.3.2 and equation 5). These light curves are displayed in Fig. 8 under the labels P4 to P8 and P9, respectively. The program does not display the light curves for alias periods outside the period range of RRLSs. The 'PLOT P-A' button plots each period with its corresponding aliases in a period-amplitude plot, as shown in the upper right-hand corner of the window in Fig. 8. This plot also shows data for RRLSs in the globular cluster M3 from Corwin & Carney (2001) as a reference to illustrate the loci occupied by RRab and RRc stars in this diagram. This plot is useful for deciding between different periods that produce similarly good period-folded light curves. In the above example, P1 was selected as the correct period. Additionally, the 'DSS' button allows downloading and plotting a DSS thumbnail image centred on the coordinates of the star, in order to facilitate the identification of contaminants like spurious extended objects, artefacts on very bright stars or double stars. Finally, the 'SAVE' button allows saving for each star, in

an ASCII format file, up to two periods, comments on each period and the variable star classification selected from the bullets in the lower left-hand part of the window.

Finally, a total of 160 RRab and 51 RRc stars were identified. As a byproduct of the visual inspection, eclipsing binary candidates were also found and will be discussed in an upcoming paper. The catalogue of  $V, R$  and  $I$  light curves for all RRab and RRc stars is shown in Fig. A1 in Appendix A. The RRLS light-curve parameters, such as amplitudes, maximum-light magnitudes and phase, were computed by fitting light-curve templates to the data using RRab and RRc templates from Layden (1998) and Vivas et al. (2008), respectively, and further refining the period with a step of  $10^{-6}$  d. These parameters are listed in Tables 6 and 7 for RRab and RRc stars, respectively.

In the following sections, we describe the effect of period aliases in the catalogue, the completeness estimated in the identification of RRLSs, as well as the possible contaminants of the sample.

### 3.3.4 Comparison with variable star catalogues

The present survey partially overlaps with the RRLS catalogue from V04 (see Fig. 1), also conducted with QUEST observations but focused on high-latitude regions. All 21 RRab stars and 31 (~78 per cent) of the RRc stars from V04, expected in our survey's area, were successfully recovered. The remaining 22 per cent of RRc stars were reclassified as contaminants based on their improved light curves which include a larger number of observations, in particular in the  $R$  and  $I$  bands, with respect to V04. The 52 RRLSs recovered from V04 keep their original identification numbers, which correspond to numbers  $\leq 999$  in Tables 6 and 7. The 27 RRLSs with identification numbers in the range 500–600 are from Vivas et al. (in preparation). The 132 RRab and RRc stars identified in the present survey have identifiers from 1000 onwards.

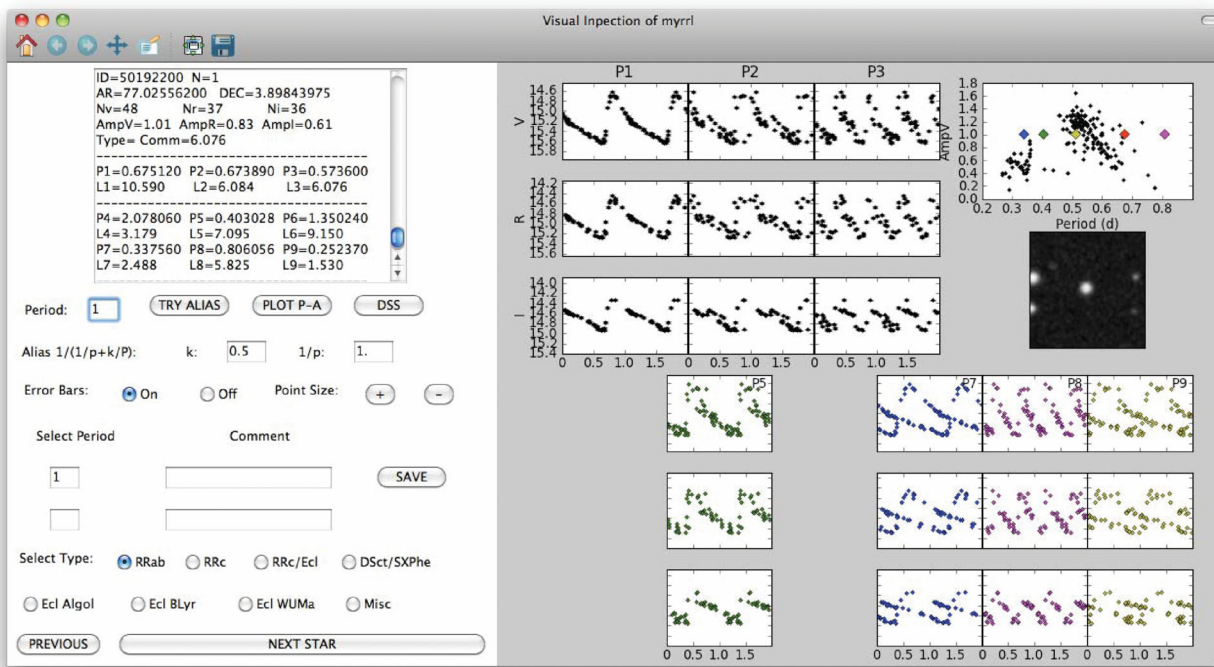


Figure 8. Graphical user interface of the `INSPECTLC.PY` tool developed for light-curve visual inspection.

**Table 6.** Light-curve parameters for RR*ab* stars. (This table is published in its entirety as Supporting Information with the electronic version of the article. A portion is shown here for guidance regarding its form and content.)

ID	$\alpha$ ( $^{\circ}$ )	$\delta$ ( $^{\circ}$ )	$(N_V, N_R, N_I)$	Period (d)	AmpV (mag)	AmpR (mag)	AmpI (mag)	HJD <sub>maxI</sub> −2450000 (d)	$\langle V \rangle$ (mag)	$\langle R \rangle$ (mag)	$\langle I \rangle$ (mag)
1000	60.935722	−1.498512	(0, 10, 9)	0.444400	–	0.91	0.62	1200.70430400	–	16.79 ± 0.02	16.55 ± 0.03
1001	62.136738	−2.995186	(0, 11, 0)	0.465461	–	0.72	–	2279.76109714	–	19.16 ± 0.11	–
1002	62.444096	−4.000918	(27, 19, 11)	0.498114	1.16	1.13	0.87	1823.74922626	17.53 ± 0.04	17.13 ± 0.02	16.49 ± 0.02
1003	65.498161	−3.226088	(28, 16, 24)	0.501271	1.25	1.07	0.87	1824.19917603	15.91 ± 0.01	15.77 ± 0.02	15.40 ± 0.01
563	66.183346	−3.859660	(24, 0, 11)	0.539828	0.85	–	0.41	1867.80606764	14.03 ± 0.02	–	13.60 ± 0.01

**Table 7.** Light-curve parameters for RR*c* stars. (This table is published in its entirety as Supporting Information with the electronic version of the article. A portion is shown here for guidance regarding its form and content.)

ID	$\alpha$ ( $^{\circ}$ )	$\delta$ ( $^{\circ}$ )	$(N_V, N_R, N_I)$	Period (d)	AmpV (mag)	AmpR (mag)	AmpI (mag)	HJD <sub>maxI</sub> −2450000 (d)	$\langle V \rangle$ (mag)	$\langle R \rangle$ (mag)	$\langle I \rangle$ (mag)
1013	74.151787	−3.740614	(21, 17, 11)	0.331910	0.43	0.40	0.23	1824.12209720	17.91 ± 0.05	17.67 ± 0.04	17.46 ± 0.05
1015	74.725197	3.882039	(44, 39, 33)	0.400277	0.58	0.36	0.23	1870.98566120	15.22 ± 0.01	14.83 ± 0.01	14.48 ± 0.01
1019	75.680612	5.070141	(19, 12, 19)	0.384742	0.38	0.38	0.33	1871.09802948	15.90 ± 0.01	15.77 ± 0.01	15.54 ± 0.03
1022	76.733847	0.805251	(33, 20, 9)	0.412460	0.44	0.37	0.16	1539.59914360	18.80 ± 0.07	18.63 ± 0.06	18.38 ± 0.10
1028	77.485196	0.078322	(82, 21, 34)	0.370848	0.30	0.22	0.14	1539.62626816	17.51 ± 0.04	17.40 ± 0.03	17.21 ± 0.05

We also cross-matched our RRLS catalogue with the ASAS-3 (Pojmanski 2002) and NSVS (Kinemuchi et al. 2006) ones, with a tolerance of 7 arcsec. Out of the 132 RRLSs not present in V04 or Vivas et al. (in preparation), 131 are new discoveries: one match is found in NSVS and none in ASAS-3. Our RRLS 1012 corresponds to star 722 of the NSVS. The period reported for this star on the NSVS is  $P_{\text{NSVS}} = 0.53495$  d which coincides within the errors with our period  $P_{\text{QUEST}} = 0.53497$  d, and in both catalogues, the star was classified as RR*ab*.

### 3.3.5 Completeness

The completeness achieved in the RRLS identification was estimated from the catalogue of synthetic light curves for RR*ab* and RR*c* stars described in Section 3.1. The completeness was computed, independently for each RRLS type, as the percentage of synthetic stars recovered after the period search described in Section 3.3.1 was performed on a sample of  $\sim 65\,000$  synthetic RRLSs of each type. A synthetic star was considered successfully recovered if one of the three best periods found was within 10 per cent of the true light-curve period or one of the period aliases described in Section 3.3.2. The average completeness was computed for synthetic stars in the magnitude range  $14.0 \leq V \leq 18.5$  as a function of position in the survey area, since it strongly depends on the time sampling and number of observations in each filter.

The resulting completeness maps for RRLSs of types RR*ab* (left-hand panel) and RR*c* (right-hand panel) are shown in Fig. 9 in equatorial coordinates. As illustrated by the figure, for RR*ab* stars the average completeness is  $\sim 95$  per cent for most of the survey area, except in the declination stripe  $-6^{\circ} \leq \delta \leq -4^{\circ}$ , where the number of observations per object is typically less than 15 in all three photometric bands (see Fig. 5). For RR*c* stars, the estimated completeness is  $\sim 80$ – $85$  per cent, significantly lower than for RR*ab* stars, as expected since RR*c* light curves have smaller amplitudes.

### 3.3.6 Possible contaminants

The main source of contamination in an RRLS survey is eclipsing binaries (mostly of WUMa type),  $\delta$  Scuti and SX Phoenicis stars. Eclipsing contact binaries or WUMa stars consist of a system in

which both stars have filled their Roche lobes and are undergoing mass transfer (Sterken & Jaschek 2005) and have light curves showing two eclipses of very similar depths.  $\delta$  Scuti stars are pulsating main-sequence dwarfs and blue stragglers, while SX Phoenicis stars are their metal-poor counterparts; both types are also called dwarf Cepheids (Nemec & Mateo 1990; Sandage & Tammann 2006) and have asymmetric light curves, similar to those of RRLSs, though with smaller periods ( $P < 0.2$  d) and amplitudes ( $\text{Amp}V \lesssim 0.2$  mag, Sterken & Jaschek 2005).

A plot of  $V$  amplitude versus period is shown in Fig. 10 for RR*ab*, RR*c*, Algol,  $\beta$  Lyrae, WUMa and  $\delta$  Scuti stars from the ASAS-3 survey (Pojmanski 2002). As illustrated by the figure, the period and amplitude ranges for most of these stars largely overlap, making the light-curve shape an important criterion in distinguishing between the different types of variables. Most of the contamination problems affect the RR*c* stars rather than the RR*ab* stars.

Eclipsing binary light curves, of any type, are unlikely to be mistaken for RRLSs of type *ab*, while dwarf Cepheids, though having similar light curves, have periods and amplitudes which are too small for RR*ab* stars. A few dwarf Cepheids could have alias periods in the range of RRLSs; however, in this case the contaminants are unlikely to follow the well-known period–amplitude relationship for RR*ab* stars (e.g. Smith 1995; Cacciari et al. 2005), which can in turn be used as a criterion to discard them. This criterion is also helpful to avoid other possible contaminants of the RR*ab* sample, such as anomalous Cepheids and short-period Type II Cepheids (Sandage & Tammann 2006), also known as BL Herculis and W Virginis stars, which have light-curve shapes similar to RR*ab* stars with periods in the range from 1 to 50 d (W Vir) and 1 to 7 d (BL Her), partially overlapping the range for RR*ab* stars in the long-period end. Therefore, the contamination expected in the RR*ab* sample can be considered negligible.

The RR*c* sample is, on the contrary, more prone to contamination. The light curves of eclipsing binaries of the WUMa and  $\beta$  Lyrae types can resemble those of RR*c* stars if period folded with half the true period of the binary. However, as noted by Kinman & Brown (2010), an important difference between RR*c* stars and eclipsing binaries is that pulsating stars have larger amplitudes in bluer bands compared to red bands, while eclipsing binaries have similar

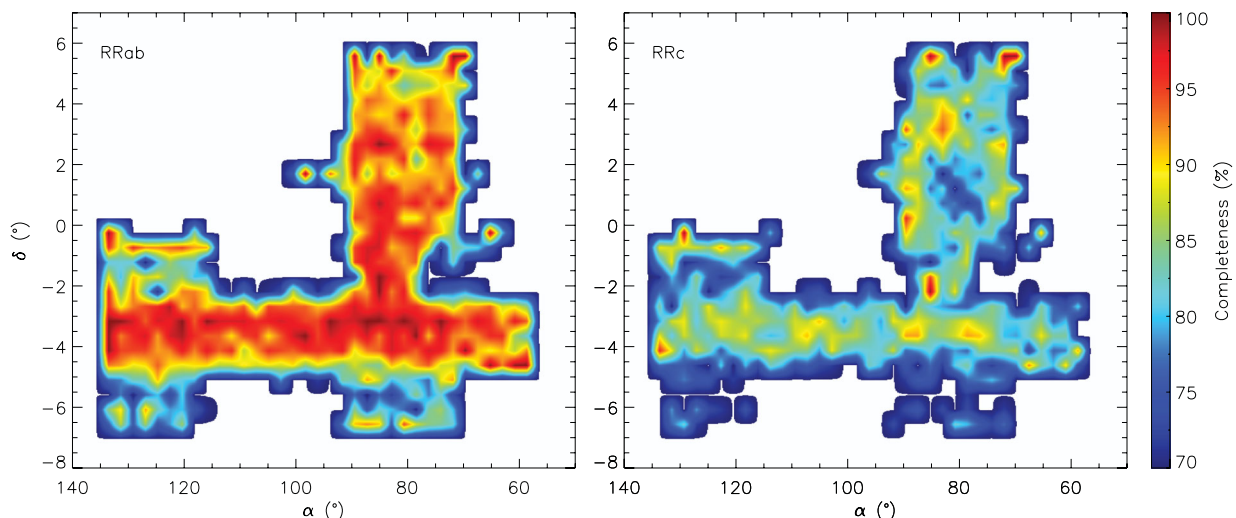


**Figure 9.** Map of average completeness in the identification of RRab (left-hand panel) and RRc (right-hand panel) stars, computed from synthetic RRLSs within the photometric completeness limits of the survey ( $14.0 \leq V \leq 18.5$ ).

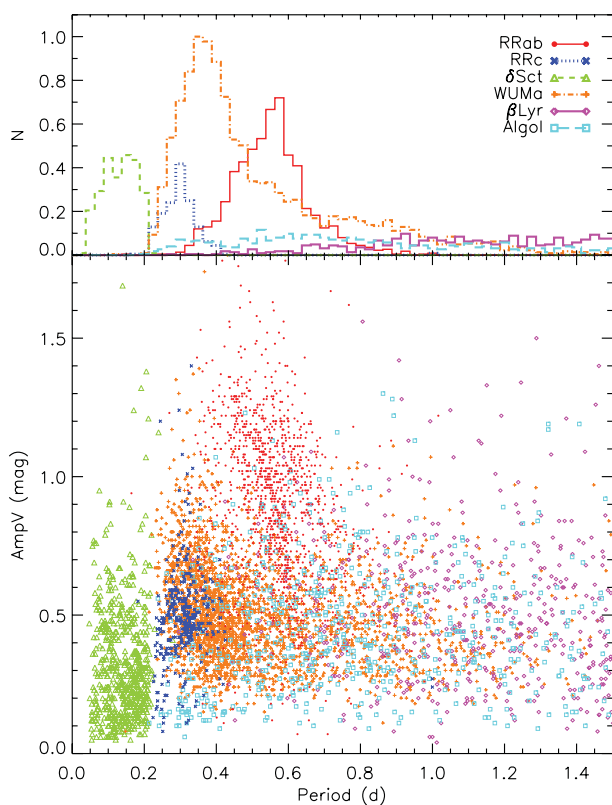


**Figure 10.** Bottom panel:  $V$  amplitude versus period for variable stars of type RRab, RRc,  $\delta$  Scuti, Algol,  $\beta$  Lyrae and WUMa from the ASAS-3 catalogue (Pojmanski 2002). Top panel: period histogram for the different variable star types illustrated in the bottom panel.

amplitudes in different photometric bands (Sterken & Jaschek 2005; Kinman & Brown 2010). This is a useful criterion for differentiating both types of variables, except for variable stars with poorly sampled light curves or very small amplitudes ( $<0.2$ – $0.3$  mag), in which case the distinction is more difficult. On the other hand, since this behaviour of the amplitude in different photometric bands is common to pulsating stars, it is not useful for distinguishing RRc stars

from the larger amplitude  $\delta$  Scuti or SX Phoenicis stars, making these likely contaminants of the sample.

Therefore, the contamination expected in the RRc sample could be significant. In particular, among the RRc, a large number of WUMa and  $\delta$  Scuti stars belonging to the thin disc are expected, given the low latitudes being surveyed and the fact that we are not imposing any colour cuts which would sizeably have reduced the contamination (Ivezić et al. 2000; V04). This added to the relatively low completeness of the RRc sample ( $\sim 80$  per cent) makes it inappropriate to use the RRc stars in the computation of the thick-disc structural parameters, which is why we have restricted the following analysis to the RRab sample.

### 3.4 Physical parameters of RRLSs

#### 3.4.1 Extinctions

The present survey spans areas at very low Galactic latitudes ( $|b| < 15^\circ$ ), where the extinction can be very high and spatially variable. The Schlegel, Finkbeiner & Davis (1998) dust maps, although covering the whole sky, are unreliable at Galactic latitudes lower than  $\sim 10^\circ$ . On the other hand, a correct estimate of the extinction is crucial in the determination of distances for the survey RRLSs and their subsequent use in the computation of density profiles.

In addition to being excellent standard candles, RRLSs can also be used as colour standards. Sturch (1966) finds the average  $B - V$  colour index during the phase of minimum light ( $\phi \in [0.5, 0.8]$ ) is approximately constant for RRab stars, having a small dispersion of  $\sim 0.03$  mag, which makes it possible to estimate the extinction affecting a particular RRab star by simply comparing the observed minimum-light colour with the intrinsic colour. Later on, the calibration was extended to  $V - I$  by Day et al. (2002) and Guldenschuh et al. (2005), and to  $V - R$  by Kunder, Chaboyer & Layden (2010), obtaining smaller standard deviations of  $\sim 0.02$  mag in these colour indices.

In the present work, we used the minimum-light colour calibrations ( $V - R)_{\min}^{0.5-0.8} = 0.27 \pm 0.02$  from Kunder et al. (2010) and  $(V - I)_{\min}^{0.5-0.8} = 0.58 \pm 0.02$  from Guldenschuh et al. (2005). For the  $\sim 40$  RRab stars that do not have  $V$ -band observations, we used the intrinsic colour  $(R - I)_{\min}^{0.5-0.8} = 0.31 \pm 0.03$ , computed from the previous two colours. The observed minimum-light colours

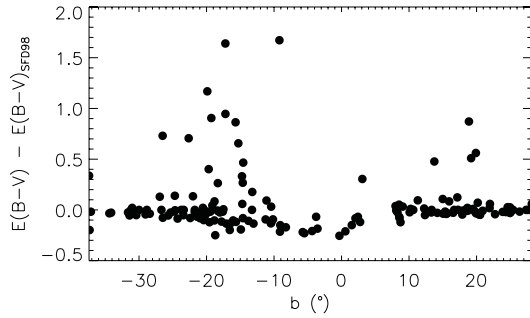


**Figure 11.** Residuals between colour excesses  $E(B - V)$  from Schlegel et al. (1998) dust maps and those computed from RRab intrinsic colours, as a function of Galactic latitude  $b$ .

were computed from the subtraction of the best-fitting templates in the two bands used. Comparing these with the assumed intrinsic colours, we computed the corresponding  $E(V - R)$ ,  $E(V - I)$  and  $E(R - I)$  colour excesses and extinctions  $A_V$ ,  $A_R$  and  $A_I$  were derived assuming the standard reddening law from Cardelli, Clayton & Mathis (1988).

We used the 56 stars with observations in all three filters to compute the residuals in the  $E(B - V)$  derived using the  $V - R$ ,  $V - I$  and  $R - I$  colour indices, in order to test the consistency of the resulting extinctions. The mean differences obtained were  $E(B - V)_{VR} - E(B - V)_{VI} = -0.007$  mag and  $E(B - V)_{RI} - E(B - V)_{VI} = -0.006$  mag, with standard deviations of 0.092 and 0.082 mag, respectively, showing there is very good agreement between the different measurements. For stars with data in the  $VRI$  filters, the adopted  $E(B - V)$  were computed as the error-weighted mean of the colour excesses computed from the  $V - R$  and  $V - I$  intrinsic colours and the corresponding errors were computed by standard error propagation.

Residuals between these colour excesses and those obtained from interpolations in the Schlegel et al. (1998) dust maps are shown in Fig. 11. The plot shows the residuals are nearly zero for moderately high Galactic latitudes ( $|b| \geq 20^\circ$ ), while as the latitude decreases the colour excesses computed from RRab intrinsic colours are systematically smaller than those from Schlegel et al. (1998). This behaviour is expected since the former correspond to the colour excesses integrated up to the distance of each RRLS, while the latter are integrated along the entire line of sight. Fig. 11 also shows larger residuals around latitudes  $b \sim -20^\circ$  and  $b \sim +10^\circ$ , which are presumably due to abrupt variations in the extinction on relatively small scales, mainly due to the presence of the Orion Molecular Cloud (at  $b \sim -20^\circ$ , see Fig. 12). The points showing the larger residuals in Fig. 11 coincide with regions where the extinction changes abruptly and the colour excesses derived from RRab stars are systematically larger than those reported by Schlegel et al. (1998), which is to be expected since the Schlegel et al. maps have relatively large pixels with  $6.1 \times 6.1$  arcmin<sup>2</sup> and abrupt variations on smaller scales will be averaged out, while RRab stars probe the extinction exactly on the line of sight towards each star.

### 3.4.2 Photometric metallicities

RRLSs of type  $ab$  exhibit a well-known relationship between metallicity  $[\text{Fe}/\text{H}]$ , pulsation period  $P$  and the  $\phi_{31}$  phase of a Fourier light-curve decomposition, discovered by Jurcsik & Kovacs (1996). Also, Sandage (2004) finds that  $\phi_{31}$  is correlated with the light-curve amplitude and finds an expression analogous to that of Jurcsik &

Kovacs (1996) relating  $[\text{Fe}/\text{H}]$  with the light-curve amplitude and period for RRab stars.

**3.4.2.1 Jurcsik & Kovacs metallicities.** Jurcsik & Kovacs (1996) found an empirical relationship between the metallicity  $[\text{Fe}/\text{H}]$ , period  $P$  and  $\phi_{31}$  phase of a Fourier decomposition of RRab light curves, expressed in their equation (3) as

$$[\text{Fe}/\text{H}] = -5.038 - 5.394P + 1.345\phi_{31}. \quad (6)$$

The dispersion in this relationship was estimated by Jurcsik & Kovacs (1996) to be 0.11 dex from a comparison with spectroscopically determined metallicities.

The Fourier fitting process is very sensitive to the light-curve sampling. For relatively well sampled curves, but with a moderate number of observations ( $N \sim 30$ ), the fits usually have excessive ripples which translate into undesirable uncertainties in the determination of  $\phi_{31}$ . In order to circumvent this problem, we used the method proposed by Kovacs & Kupi (2007) which consists of fitting an observed light curve with one of their 248 light-curve templates, representative of RRab stars, and determining  $\phi_{31}$  from the Fourier decomposition of the best-fitting template.<sup>6</sup> This allows for robust Fourier decompositions of light curves with a moderate number of observations ( $N \gtrsim 20$ ). In order to have an estimate of the quality of the fit, we use the  $D_F$  index defined by Jurcsik & Kovacs (1996), which tests for consistency of the Fourier decomposition parameters using the fact that different Fourier phases  $\phi_{ij}$  are correlated (see their table 6). The restriction  $D_F < 3$  was applied in order to ensure the reliability of the Fourier fits used in the computation of metallicities, as suggested by Jurcsik & Kovacs (1996).

**3.4.2.2 Sandage metallicities.** Using a sample of RRab stars having spectroscopically derived metallicities, Sandage (2004) finds the following empirical relationship between  $[\text{Fe}/\text{H}]$ , light-curve period and amplitude:

$$[\text{Fe}/\text{H}]_V = (-1.45 \pm 0.04)\text{Amp}_V - (7.99 \pm 0.09) \log P - (2.145 \pm 0.025) \quad (7)$$

Sandage argues this relationship reflects the same behaviour as found by Jurcsik & Kovacs (1996), since  $\phi_{31}$  correlates directly with the light-curve amplitude. In practice, Sandage's relation can be used in many more RRLS catalogues since it only requires an accurate knowledge of period and amplitude, while in order to perform the Fourier fits of Jurcsik & Kovacs (1996) the full time series data are required and the light curves must have an appropriate time sampling.

The relationship expressed in equation (7) is calibrated for the  $V$  band, found in the majority of RRLS observations in the literature. In our catalogue of 160 RRab stars, 25 per cent of the stars have observations only in the  $R$  and/or  $I$  bands and not in  $V$ , which made it necessary to extend Sandage's relation for these photometric bands. Using the photometric metallicities computed from equation (7) for 49 of our stars which are well observed in  $V$  and  $R$  ( $N_V \geq 20$  and  $N_R \geq 20$ ) and 45 stars in  $V$  and  $I$  ( $N_V \geq 20$  and  $N_I \geq 20$ ), we obtained analogous equations for the  $R$  and  $I$  bands, via least-squares fitting of the corresponding metallicities, periods and amplitudes. The corresponding equations are

$$[\text{Fe}/\text{H}]_R = (-1.052 \pm 0.027)\text{Amp}_R - (6.281 \pm 0.087) \log P - (2.254 \pm 0.028), \quad (8)$$

<sup>6</sup> We used the `TFEF` software from Kovacs & Kupi (2007) in the template-fitting and Fourier decomposition processes.

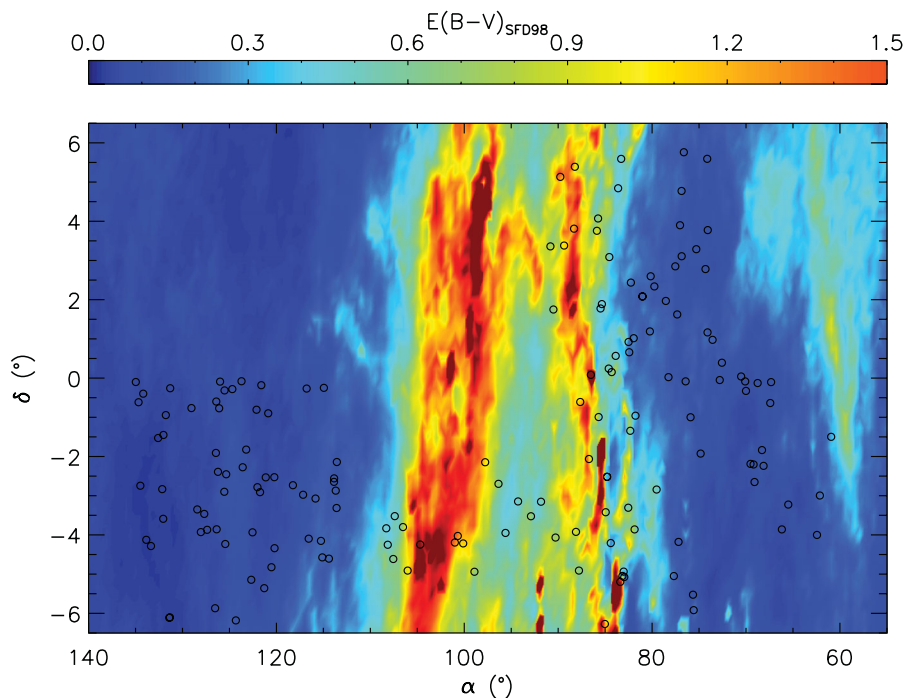


**Figure 12.**  $E(B - V)$  map from Schlegel et al. (1998). The open circles indicate survey RRab stars.

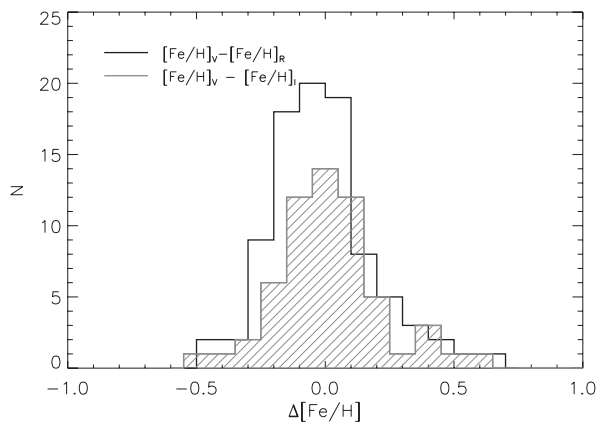


**Figure 13.** Distribution of differences for photometric metallicities  $[\text{Fe}/\text{H}]_R$  and  $[\text{Fe}/\text{H}]_I$  computed from  $R$ - and  $I$ -band amplitudes (equations 8 and 9), with respect to  $[\text{Fe}/\text{H}]_V$ , computed from the  $V$ -band amplitude (equation 7).

$$[\text{Fe}/\text{H}]_I = (-1.469 \pm 0.032)\text{Amp}_I - (6.516 \pm 0.091) \log P - (2.250 \pm 0.027). \quad (9)$$

Fig. 13 shows the distribution of residuals of photometric metallicities  $[\text{Fe}/\text{H}]_R$  and  $[\text{Fe}/\text{H}]_I$  computed from the  $R$ - and  $I$ -band amplitudes and equations (8) and (9), respectively, with respect to  $[\text{Fe}/\text{H}]_V$  derived from equation (7) (Sandage 2004). The two distributions show the agreement between the photometric metallicities computed from equations (8) and (9) derived in this work, and those computed via equation (7) from Sandage (2004), resulting in mean residuals of  $-0.01$  and  $0.006$  dex, respectively. The intrinsic dispersion of photometric metallicities computed from equation (7), in comparison with spectroscopic metallicities, was estimated by Sandage (2004) as  $\sigma_{[\text{Fe}/\text{H}]_V}^V = 0.26$ . Standard deviations for the residual distributions in Fig. 13 were found to be 0.19 and 0.17 dex for metallicities computed from  $R$ - and  $I$ -band amplitudes, respectively.

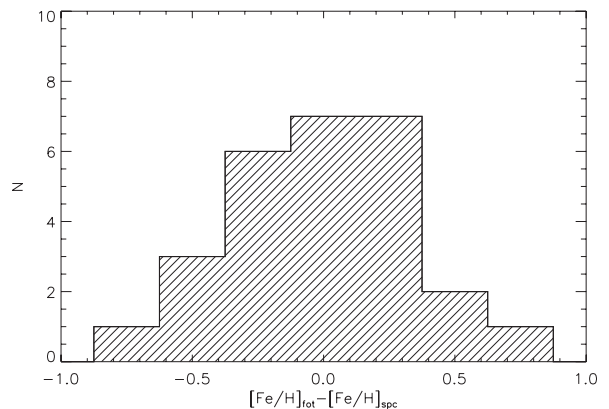


**Figure 14.** Distribution of residuals of photometric  $[\text{Fe}/\text{H}]_{\text{rot}}$  and spectroscopic  $[\text{Fe}/\text{H}]_{\text{spc}}$  metallicities for 27 RRab in the Vivas et al. (2008) catalogue.

Adding these dispersions in quadrature with  $\sigma_{[\text{Fe}/\text{H}]_V}^V$ , we estimated the intrinsic dispersion of equations (8) and (9) to be  $\sigma_{[\text{Fe}/\text{H}]_R}^R = 0.32$  and  $\sigma_{[\text{Fe}/\text{H}]_I}^I = 0.31$  dex, respectively. Uncertainties in the reported photometric metallicities were computed by adding in quadrature the errors obtained from error propagation in equations (7)–(9) with the respective intrinsic dispersion of each equation. Using these procedures, the first term accounts for the amplitude uncertainty (the contribution of period uncertainties is negligible), while the second term accounts for the intrinsic dispersion of the method. The typical uncertainties obtained for the photometric metallicities are  $\sim 0.4$  dex.

An additional test on these methods was performed by comparing the spectroscopic metallicities for 27 RRab stars from the Vivas et al. (2008) catalogue, with the corresponding photometric metallicities computed from equation (7). Fig. 14 shows the resulting distribution of residuals  $[\text{Fe}/\text{H}]_{\text{rot}} - [\text{Fe}/\text{H}]_{\text{spc}}$ . The mean and standard deviation

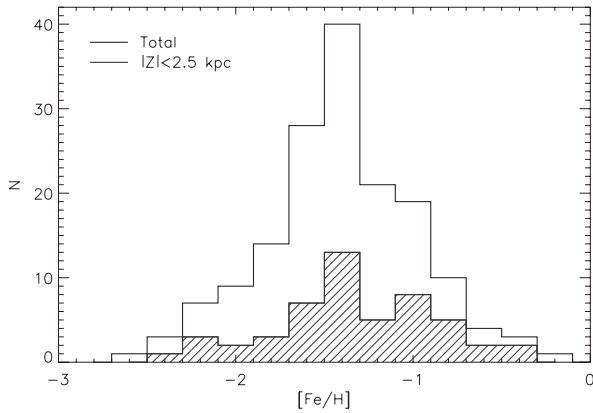


**Figure 15.** Photometric metallicity distribution for the 160 RRab stars in the survey (black). The filled histogram (blue) shows the distribution of metallicities for stars near the Galactic plane with  $|z| \leq 2.5$  kpc.

of these residuals are  $-0.01$  and  $0.34$  dex, respectively, in agreement with the intrinsic dispersions for equations (7)–(9).

**3.4.2.3 Metallicity distribution.** The photometric metallicities adopted for RRab stars were calculated from a weighted average of the metallicities computed using the Jurcsik & Kovacs (1996) (equation 6) and Sandage (2004) (equation 7–9) methods. For those stars for which the Fourier decomposition obtained was unreliable (i.e.  $D_F > 3$ ), the metallicity computed from Sandage’s method was adopted. The metallicities reported here are on the Zinn & West (1984) scale, and for all stars lie inside the metallicity range ( $-2.5 \leq [\text{Fe}/\text{H}] \leq +0.07$ ) of the stars used in the calibration of the Jurcsik & Kovacs (1996) and Sandage (2004) methods.

The distribution of metallicities obtained is shown in Fig. 15, for the full RRab sample (black) and for the stars close to the Galactic plane with  $|z| \leq 2.5$  kpc. The total metallicity distribution extends from  $[\text{Fe}/\text{H}] \sim -2.5$  up to  $[\text{Fe}/\text{H}] \sim +0.5$  with a mode at  $[\text{Fe}/\text{H}] \sim -1.48$  as can be seen in the figure. The main peak coincides with the expected peak of the halo metallicity distribution, which has an observed metallicity  $[\text{Fe}/\text{H}] = -1.5$  according to Carney, Latham, Laird & Aguilar (1994) and Layden (1995), for F and G field halo dwarfs and RRLSs, respectively. The metallicity distribution near the Galactic plane shows a hint of an excess for  $[\text{Fe}/\text{H}] \gtrsim -1.0$ , around the metallicity expected for thick-disc stars around  $[\text{Fe}/\text{H}] \sim -0.8$  (Gilmore, Wyse & Jones 1995; Layden 1995).

### 3.4.3 Distances

The computation of heliocentric distances for the RRab stars was done using absolute magnitudes  $M_V^{\text{RRL}}$  and  $M_I^{\text{RRL}}$  derived from the period–luminosity–metallicity relations in Catelan, Pritzl & Smith (2004, their equations 8 and 3, respectively). According to Catelan et al. (2004) the use of period–luminosity–metallicity relations is preferable over  $M_V$ – $[\text{Fe}/\text{H}]$  relations, since the former allow accounting for evolution off the zero-age horizontal branch. The total metal abundance  $Z$  was computed from  $[\text{Fe}/\text{H}]$  using equation (10) in Catelan et al. (2004), assuming an  $\alpha$  to Fe abundance of  $[\alpha/\text{Fe}] = 0.2$  dex typical of halo and thick-disc stars (e.g. Reddy et al. 2003; Venn et al. 2004). For the nine RRab stars which only have  $R$ -band photometry, we computed  $M_R^{\text{RRL}}$  by interpolating the corresponding coefficients in table 4 of Catelan et al. (2004).

Finally, the heliocentric distances were computed from Pogson’s equation  $\log R_{\text{hel}} = (m_i - A_i - M_i + 5)/5$ , where  $A_i$ ,  $M_i$  and  $m_i$

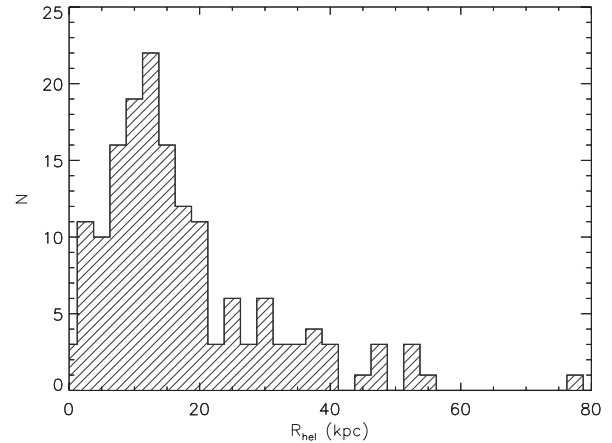


**Figure 16.** Distribution of heliocentric distances of survey RRab stars.

**Table 8.** Distances, colour excesses and metallicities for RRab stars. (This table is published in its entirety as Supporting Information with the electronic version of the article. A portion is shown here for guidance regarding its form and content.)

ID	$E(B - V)$ (mag)	$[\text{Fe}/\text{H}]$ (dex)	$R_{\text{hel}}$ (kpc)	$z$ (kpc)	$R$ (kpc)
1000	0.02	$-1.0 \pm 0.3$	$17.1 \pm 1.3$	$-10.4 \pm 0.8$	$21.5 \pm 1.0$
1001	0.13	$-0.9 \pm 0.3$	$46.4 \pm 2.5$	$-28.0 \pm 1.5$	$44.8 \pm 1.9$
1002	0.41	$-1.4 \pm 0.5$	$13.0 \pm 1.7$	$-7.9 \pm 1.0$	$18.1 \pm 1.3$
1003	0.01	$-1.6 \pm 0.1$	$11.5 \pm 0.8$	$-6.5 \pm 0.5$	$17.3 \pm 0.6$
563	0.01	$-2.1 \pm 0.1$	$5.0 \pm 0.2$	$-2.8 \pm 0.1$	$12.0 \pm 0.2$

correspond to the extinction, observed and absolute magnitudes, respectively, in the  $i$  filter. The corresponding errors were computed via error propagation in this equation, resulting in typical distance errors of  $\sim 7$  per cent. The resulting heliocentric distance distribution is shown in Fig. 16 and spans the range  $0.2 \leq R_{\text{hel}}(\text{kpc}) \leq 80$ . In Table 8, we summarize the colour excesses, metallicities, heliocentric distances  $R_{\text{hel}}$ , as well as height above the plane  $z$  and radial distance  $R$  projected on the Galactic plane, obtained for all RRab stars.

## 4 SUMMARY

We have presented the QUEST RR Lyrae Survey at low Galactic latitude, which spans an area of  $476 \text{ deg}^2$  on the sky, with multi-epoch observations in the  $V$ ,  $R$  and  $I$  photometric bands for  $6.5 \times 10^6$  stars in the Galactic latitude range  $-30^\circ \leq b \leq +25^\circ$ . The survey has a mean number of 30 observations per object in each of the  $V$  and  $I$  bands and  $\sim 25$  in the  $R$  band, while in the best sampled areas each object can have up to  $\sim 120$ – $150$  epochs in  $V$  and  $I$  and up to  $\sim 100$  in  $R$ . The completeness magnitudes of the survey are  $V = 18.5$  mag,  $R = 18.5$  mag and  $I = 18.0$  mag with saturations of  $V = R = 14.0$  mag and  $I = 13.5$  mag.

The survey has identified 211 RRLSs, 160 bona fide stars of type  $ab$  and 51 strong candidates of type  $c$ . The RRLS catalogue presented here contains the positions, mean magnitudes in  $VRI$ , periods, amplitudes, photometric metallicities, distances and individual extinctions computed from minimum light colours for each star, as well as the period-folded light curves for RRab stars (Tables 6, 7, 8 and Fig. A1). The typical distance errors obtained were  $\sim 7$  per cent. The completeness of the RRLS survey was estimated in  $\gtrsim 95$  per cent for RRab and  $\sim 85$  per cent for RRc stars, and was

computed from light-curve simulations reproducing the time sampling and other observing characteristics of our survey, as well as the variable identification and period searching techniques used.

Our RRLS survey spans *simultaneously* a large range of heliocentric distances  $0.5 \leq R_{\text{hel}}(\text{kpc}) \leq 40$  and heights above the plane  $-15 \leq z(\text{kpc}) \leq +20$ , with well-characterized completeness across the survey area. Combining ours with a bright RRLS survey (such as those from Layden 1995; Maintz 2005, see Section 1) to increase the distance coverage even further will result in a very good tool for studying the Galactic thick disc's structure, in particular for the determination of the density profile's scalelength, scaleheight as well as their dependence on radial distance in order to explore the flare and the truncation profile of the thick disc. This way the QUEST RRLSs from this work will help put constraints on the structure of the more external parts of the thick disc towards the anticentre, as well as the mechanisms that could have contributed to the formation of the Galactic thick disc. These issues will be addressed in detail in an upcoming paper of the series.

## ACKNOWLEDGMENTS

This research was based on observations collected at the Jürgen Stock 1-m Schmidt telescope of the National Observatory of Llano del Hato Venezuela (NOV), which is operated by CIDA for the Ministerio del Poder Popular para Ciencia y Tecnología, Venezuela. The facilities of the 0.9-m telescope of the SMARTS Consortium and the YALO telescope at CTIO, Chile, were also used. CM is pleased to thank Gladis Magris, Gustavo Bruzual and Carlos Abad for stimulating and helpful discussions. CM acknowledges the support from doctoral grants of the Academia Nacional de Ciencias Físicas, Matemáticas y Naturales of Venezuela and CIDA. The work reported here was supported in part by grant S1-2001001144 from FONACIT, Venezuela. RZ acknowledges the support of NSF grant AST-1108948 from the US government. The authors are grateful for the assistance of the personnel, service-mode observers, telescope operators and technical staff at CIDA and CTIO, who made possible the acquisition of photometric observations at the NOV and SMARTS telescopes. The software package TOPCAT (<http://www.starlink.ac.uk/topcat/>) was used extensively in the preparation of this paper.

## REFERENCES

- Alcock C. et al., 1999, *PASP*, 111, 1539  
 Alcock C. et al., 2003, *ApJ*, 598, 597  
 Baltay C. et al., 2002, *PASP*, 114, 780  
 Bensby T., Zenn A. R., Oey M. S., Feltzing S., 2007, *ApJ*, 663, L13  
 Bovy J., Rix H.-W., Hogg D. W., 2012a, *ApJ*, 751, 131  
 Bovy J., Rix H.-W., Liu C., Hogg D. W., Beers T. C., Lee Y. S., 2012b, *ApJ*, 753, 148  
 Briceño C., Calvet N., Vivas A. K., Hartmann L., 2003, *Mem. Soc. Astron. Ital.*, 74, 870  
 Briceño C., Calvet N., Hernández J., Vivas A. K., Hartmann L., Downes J. J., Berlind P., 2005, *AJ*, 129, 907  
 Brown W. R., Beers T. C., Wilhelm R., Prieto C. A., Geller M. J., Kenyon S. J., Kurtz M. J., 2008, *AJ*, 135, 564  
 Cabrera-Lavers A., Garzón F., Hammersley P. L., 2005, *A&A*, 433, 173  
 Cacciari C., Corwin T. M., Carney B. W., 2005, *AJ*, 129, 267  
 Cardelli J. A., Clayton G. C., Mathis J. S., 1988, *ApJ*, 329, L33  
 Carney B. W., Latham D. W., Laird J. B., Aguilar L. A., 1994, *AJ*, 107, 2240  
 Carollo D. et al., 2010, *ApJ*, 712, 692  
 Catelan M., Pritzl B. J., Smith H. A., 2004, *ApJS*, 154, 633  
 Chen Y. Q., Zhao G., Carrell K., Zhao J. K., 2011, *AJ*, 142, 184  
 Chiba M., Beers T. C., 2000, *AJ*, 119, 2843  
 Corwin T. M., Carney B. W., 2001, *AJ*, 122, 3183  
 Day A. S. et al., 2002, *PASP*, 114, 645  
 deJong J. T. A., Yanny B., Rix H.-W., Dolphin A. E., Martin N. F., Beers T. C., 2010, *ApJ*, 714, 663  
 Demarque P., Zinn R., Lee Y.-W., Yi S., 2000, *AJ*, 119, 1398  
 Dorfi E. A., Feuchtinger M. U., 1999, *A&A*, 348, 815  
 Gilmore G., Wyse R. F. G., Jones J. B., 1995, *AJ*, 109, 1095  
 Guldenschuh K. A. et al., 2005, *PASP*, 117, 721  
 Hammersley P. L., López-Corredoira M., 2011, *A&A*, 527, 6  
 Hartman J. D., Bakos G., Stanek K. Z., Noyes R. W., 2004, *AJ*, 128, 1761  
 Ivezić Ž. et al., 2000, *AJ*, 120, 963  
 Ivezić Ž., Vivas A. K., Lupton R. H., Zinn R., 2005, *AJ*, 129, 1096  
 Jurcsik J., Kovacs G., 1996, *A&A*, 312, 111  
 Jurić M. et al., 2008, *ApJ*, 673, 864  
 Katz D., Soubiran C., Cayrel R., Barbuy B., Friel E., Bienayme O., Perrin M.-N., 2011, *A&A*, 525, 90  
 Keller S. C., Murphy S., Prior S., Costa G. D., Schmidt B., 2008, *ApJ*, 678, 851  
 Kenyon S. J., Hartmann L., 1995, *ApJS*, 101, 117  
 Kinemuchi K., Smith H. A., Woźniak P. R., McKay T. A., 2006, *AJ*, 132, 1202  
 Kinman T. D., Brown W. R., 2010, *AJ*, 139, 2014  
 Kovacs G., 2009, in Guzik J. A., Bradley P. A., eds, *AIP Conf. Ser. Vol. 1170, Stellar Pulsation: Challenges for Theory and Observation*. Am. Inst. Phys., New York, p. 261  
 Kovacs G., Kupi G., 2007, *A&A*, 462, 1007  
 Kunder A., Chaboyer B., 2008, *AJ*, 136, 2441  
 Kunder A., Chaboyer B., Layden A., 2010, *AJ*, 139, 415  
 Laffler J., Kinman T. D., 1965, *ApJS*, 11, 216  
 Larsen J. A., Humphreys R. M., 2003, *AJ*, 125, 1958  
 Layden A. C., 1994, *AJ*, 108, 1016  
 Layden A. C., 1995, *AJ*, 110, 2288  
 Layden A. C., 1998, *AJ*, 115, 193  
 López-Corredoira M., Cabrera-Lavers A., Garzón F., Hammersley P. L., 2002, *A&A*, 394, 883  
 Maintz G., 2005, *A&A*, 442, 381  
 Maintz G., de Boer K. S., 2005, *A&A*, 442, 229  
 Martin J. C., Morrison H. L., 1998, *AJ*, 116, 1724  
 Miceli A. et al., 2008, *ApJ*, 678, 865  
 Momany Y., Zaggia S., Gilmore G., Piotto G., Carraro G., Bedin L. R., de Angeli F., 2006, *A&A*, 451, 515  
 Monet D. G., 1998, *BAAS*, 193, 1427  
 Nemeč J., Mateo M., 1990, in Cacciari C., Clementini G., eds, *ASP Conf. Ser. Vol. 11, Confrontation Between Stellar Pulsation and Evolution*. Astron. Soc. Pac., San Francisco, p. 64  
 Ojha D. K., 2001, *MNRAS*, 322, 426  
 Pojmanski G., 2002, *Acta Astron.*, 52, 397  
 Reddy B. E., Lambert D. L., 2008, *MNRAS*, 391, 95  
 Reddy B. E., Tomkin J., Lambert D. L., Prieto C. A., 2003, *MNRAS*, 340, 304  
 Reddy B. E., Lambert D. L., Prieto C. A., 2006, *MNRAS*, 367, 1329  
 Rengstorf A. W. et al., 2004, *ApJ*, 617, 184  
 Robin A. C., Haywood M., Creze M., Ojha D. K., Bienayme O., 1996, *A&A*, 305, 125  
 Sandage A., 2004, *AJ*, 128, 858  
 Sandage A., Tammann G. A., 2006, *ARA&A*, 44, 93  
 Schlegel D. J., Finkbeiner D. P., Davis M., 1998, *ApJ*, 500, 525  
 Sesar B., Vivas A. K., Duffau S., Ivezić Ž., 2010, *ApJ*, 717, 133  
 Siegel M. H., Majewski S. R., Reid N., Thompson I. B., 2002, *ApJ*, 578, 151  
 Smith H. A., 1995, *RR Lyrae Stars*. Cambridge Univ. Press, Cambridge  
 Soszynski I. et al., 2011, *Acta Astron.*, 61, 1  
 Soubiran C., Bienayme O., Siebert A., 2003, *A&A*, 398, 141  
 Sterken C., Jaschek C., 2005, *Light Curves of Variable Stars*. Cambridge Univ. Press, Cambridge  
 Stetson P. B., 1987, *PASP*, 99, 191  
 Stetson P. B., 1996, *PASP*, 108, 851  
 Sturch C., 1966, *AJ*, 143, 774



Venn K. A., Irwin M., Shetrone M. D., Tout C. A., Hill V., Tolstoy E., 2004, *AJ*, 128, 1177  
 Vivas A. K. et al., 2004, *AJ*, 127, 1158 (V04)  
 Vivas A. K., Jaffé Y. L., Zinn R., Winnick R., Duffau S., Mateu C., 2008, *AJ*, 136, 1645  
 Watkins L. L. et al., 2009, *MNRAS*, 398, 1757  
 Welch D. L., Stetson P. B., 1993, *AJ*, 105, 1813  
 Wyse R. F. G., 2009, in Andersen J., Bland-Hawthorn J., Nordstrom B., eds, *IAU Symp. 254, The Galaxy Disk in Cosmological Context*. Cambridge Univ. Press, Cambridge, p. 179

Yoachim P., Dalcanton J. J., 2006, *AJ*, 131, 226  
 Zinn R., West M. J., 1984, *ApJS*, 55, 45

## APPENDIX A: RRLS LIGHT CURVES

The catalogue of *V*, *R* and *I* period-folded light curves for all RRab and RRc stars found by the survey is shown in Fig. A1.

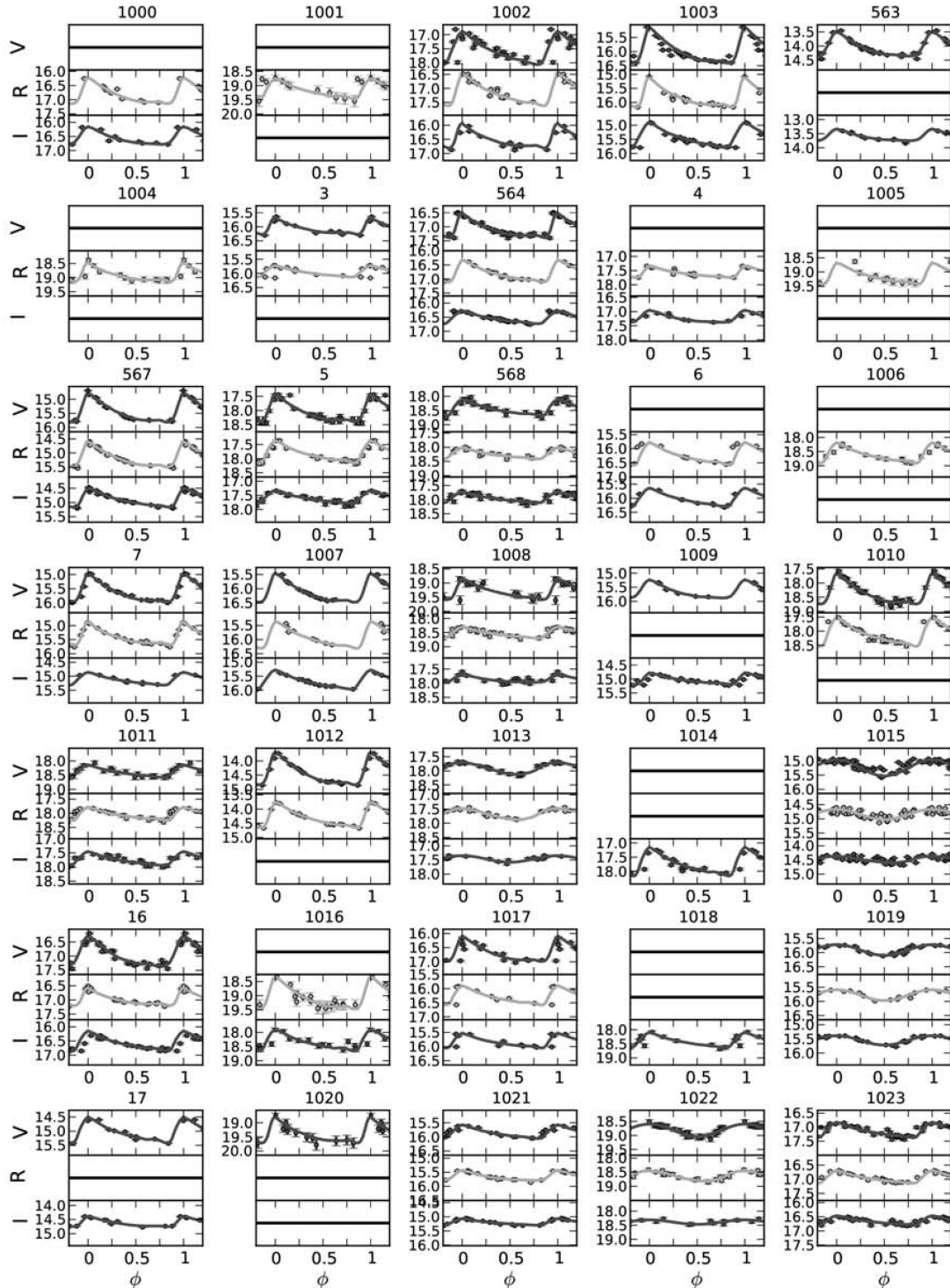


Figure A1. Light curves of survey RRab and RRc stars.

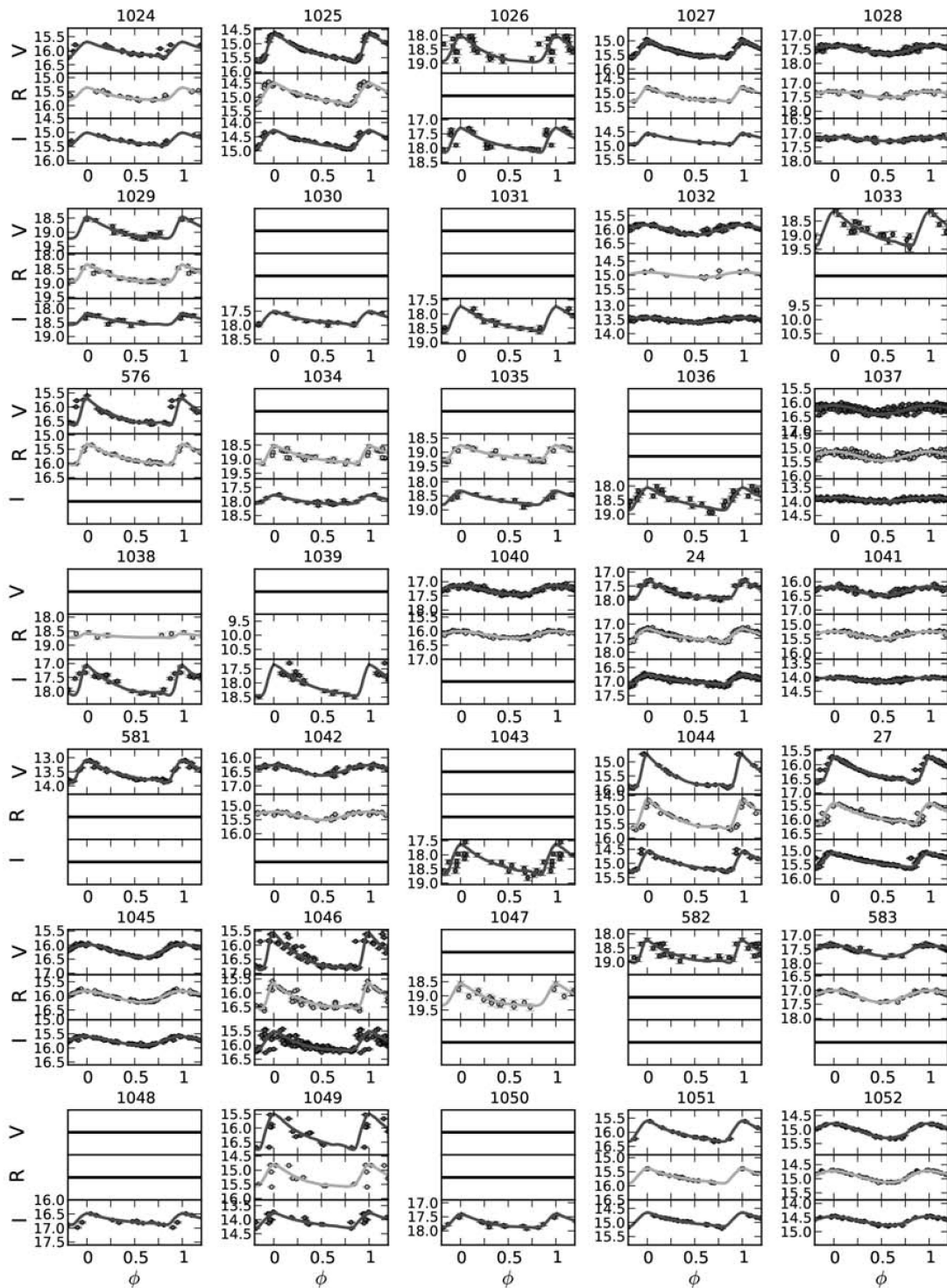
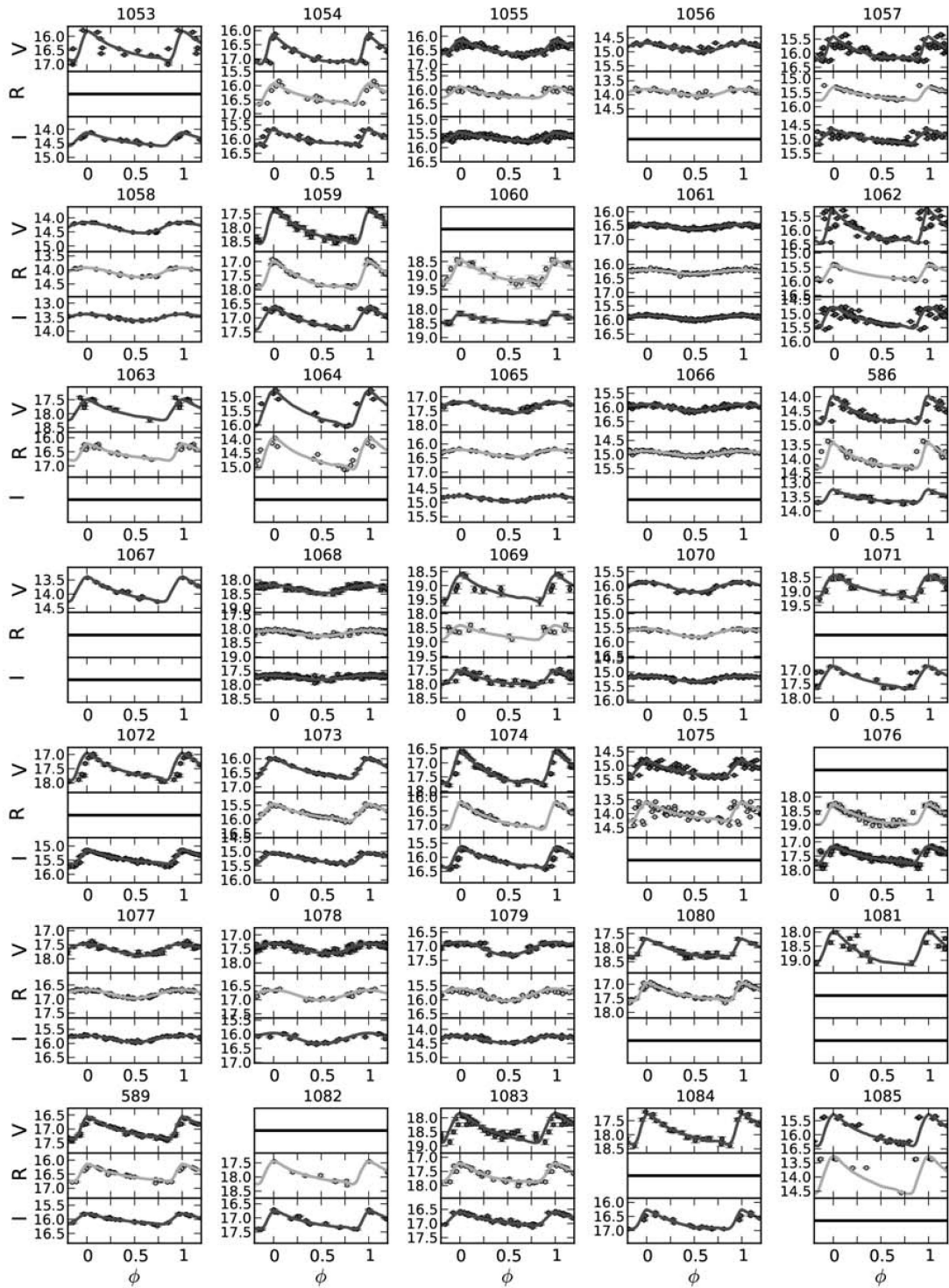


Figure A1 – continued.

Figure A1 – *continued.*

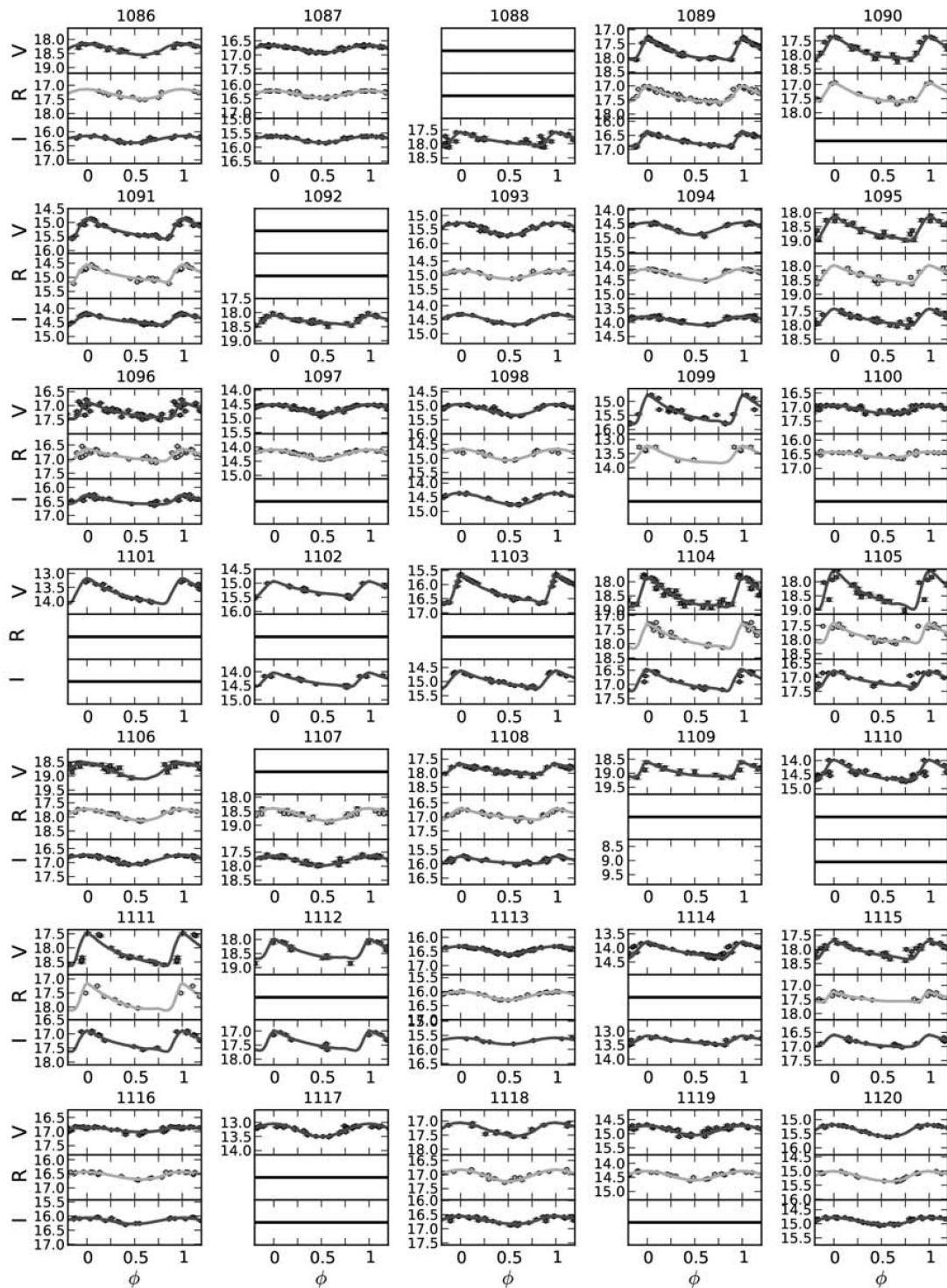


Figure A1 – continued.

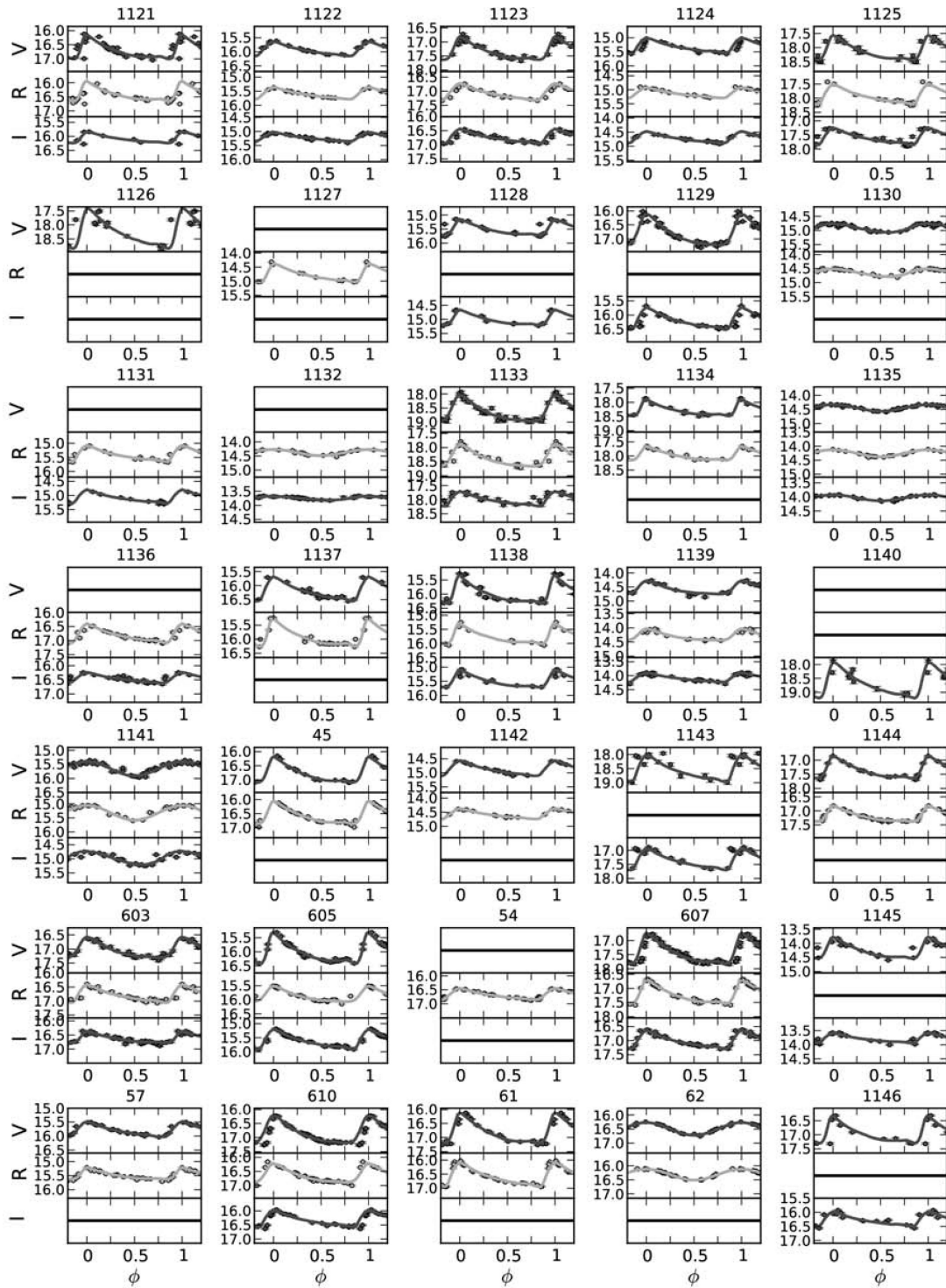


Figure A1 – *continued.*

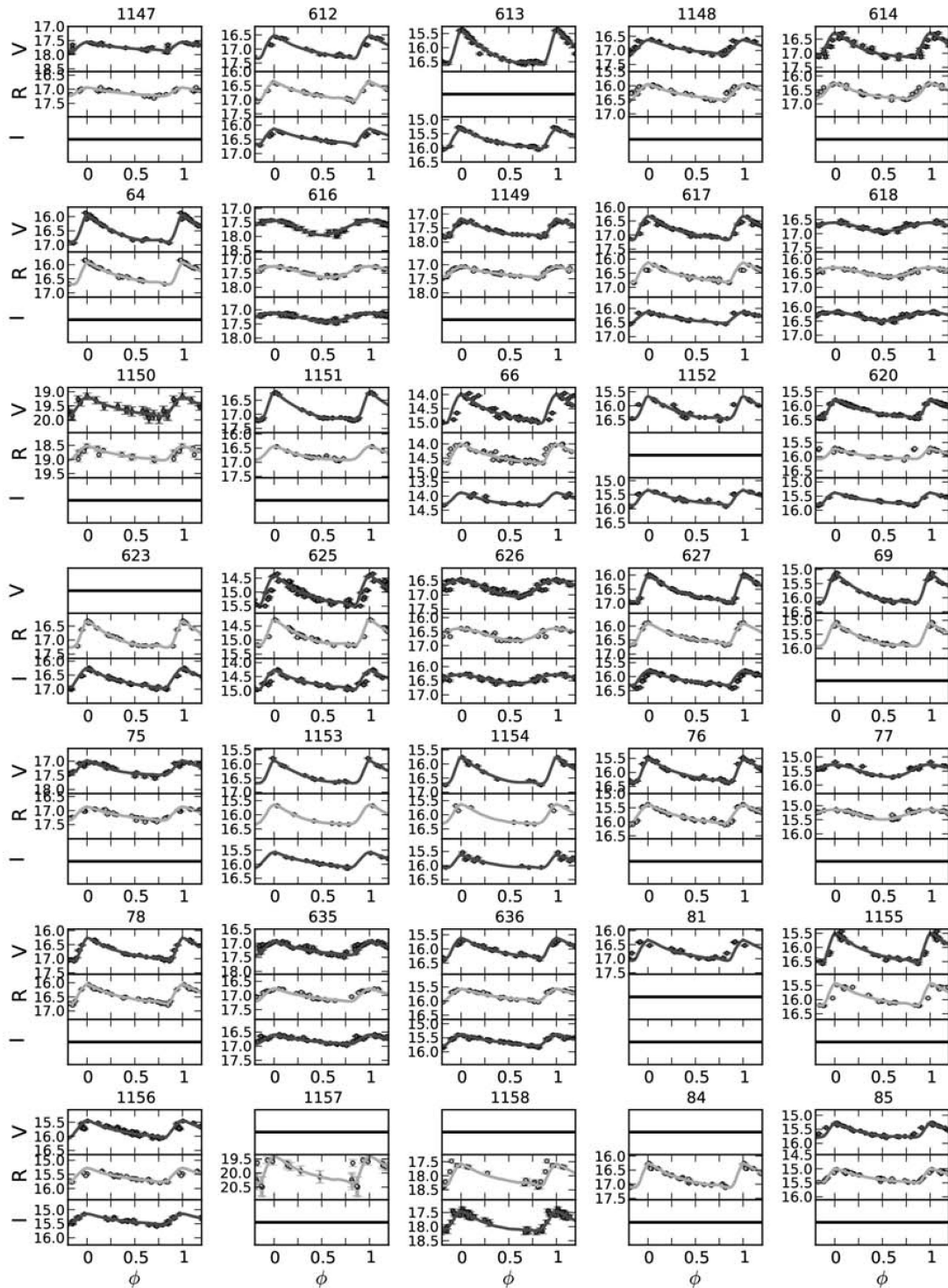


Figure A1 – continued.

## SUPPORTING INFORMATION

Additional Supporting Information may be found in the online version of this article:

**Table 2.** Magnitudes for second-order photometric standards.

**Table 6.** Light-curve parameters for RRab stars.

**Table 7.** Light-curve parameters for RRc stars.

**Table 8.** Distances, colour excesses and metallicities for RRab stars.

Please note: Wiley-Blackwell are not responsible for the content or functionality of any supporting materials supplied by the authors. Any queries (other than missing material) should be directed to the corresponding author for the article.

This paper has been typeset from a  $\text{\TeX}/\text{\LaTeX}$  file prepared by the author.